The Tropical Diurnal Cycle Under Varying States of the Monsoonal Background Wind

Michael B. Natoli [a] Eric D. Maloney,[a]

[a] *Colorado State University, Fort Collins, CO*

Corresponding author: Michael B. Natoli, mbnatoli@colostate.edu

ABSTRACT: The impact of the environmental background wind on the diurnal cycle near tropical islands is examined in observations and an idealized model. Luzon Island in the northern Philippines is used as an observational test case. Composite diurnal cycles of CMORPH precipitation are constructed based on an index derived from the first empirical orthogonal function (EOF) of ERA5 zonal wind profiles. A strong precipitation diurnal cycle and pronounced offshore propagation in the leeward direction tends to occur on days with a weak, offshore prevailing wind. Strong background winds, particularly in the onshore direction, are associated with a suppressed diurnal cycle. Idealized high resolution 2-D Cloud Model 1 (CM1) simulations test the dependence of the diurnal cycle on environmental wind speed and direction by nudging the model base-state toward composite profiles derived from the reanalysis zonal wind index. These simulations can qualitatively replicate the observed development, strength, and offshore propagation of diurnally generated convection under varying wind regimes. Under strong background winds, the land-sea contrast is reduced, which leads to a substantial reduction in the strength of the sea-breeze circulation and precipitation diurnal cycle. Weak offshore prevailing winds favor a strong diurnal cycle and offshore leeward propagation, with the direction of propagation highly sensitive to the background wind in the lower free troposphere. Offshore propagation speed appears consistent with density current theory rather than a direct coupling to a single gravity wave mode, though several gravity wave modes apparent in the model likely contribute to a destabilization of the offshore environment.

1. Introduction

Variability in the diurnal cycle can be a critical factor in determining total precipitation on the islands and in coastal waters of the Maritime Continent (MC; Biasutti et al. 2012; Bergemann et al. 2015; Zhu et al. 2017). The warm sea surface temperatures (SSTs), numerous islands of varying size, and complex topography make understanding the abundant precipitation in this region a challenging problem with global ramifications (Ramage 1968; Neale and Slingo 2003). The diurnal cycle is also critical for the development of extreme rainfall and the high mean-state rainfall found in coastal oceans (Ruppert and Chen 2020). While the diurnal cycle has been extensively studied, uncertainty remains regarding its variability and response to large-scale controls.

The canonical diurnal cycle behavior over MC islands develops from convergence associated with the sea-breeze or mountain-breeze in the late morning, typically contributing maximum precipitation rates in the late afternoon and evening hours (Dai 2001; Kikuchi and Wang 2008). Frequently, convection will then propagate offshore during the overnight hours, leading to an overnight or morning maximum in precipitation rates over coastal oceanic regions (Yang and Slingo 2001; Mori et al. 2004; Sakurai et al. 2005; Natoli and Maloney 2019). Offshore propagation has been attributed to convergence associated with the land-breeze (e.g. Houze et al. 1981; Ho et al. 2008; Fujita et al. 2011), advection by the mean wind (e.g. Ichikawa and Yasunari 2006, 2008; Yanase et al. 2017), and destabilization of the offshore environment by low-level ascent initiated by gravity waves (e.g. Mapes et al. 2003; Love et al. 2011; Hassim et al. 2016; Yokoi et al. 2017). Diurnal cycle behavior and the tendency for offshore propagation varies widely from one day to the next, motivating continued research. The MC region is also influenced by numerous large-scale modes of variability from features on global, inter-annual time scales like the El Niño Southern Oscillation (ENSO; Rauniyar and Walsh 2013) or Indian Ocean Dipole (IOD; **?** to equatorial waves on synoptic scales (Ferrett et al. 2019). Any of these can significantly affect the diurnal cycle and local precipitation (Sakaeda et al. 2020; Natoli and Maloney 2021).

The Madden-Julian Oscillation (MJO; Madden and Julian 1971, 1972) impact on the diurnal cycle has been one of the more widely studied relationships, in part because of the potential for the diurnal cycle to feed back onto MJO propagation across the MC (Oh et al. 2013; Peatman et al. 2014; Hagos et al. 2016). The MJO is an eastward-propagating area of enhanced convection in the tropical warm pool with a time-scale of 30-90 days. The active phase is characterized by strong westerly winds and abundant free-tropospheric moisture, while the suppressed phase exhibits easterly winds, a dry free-troposphere, and sunnier skies (Madden and Julian 1994; Maloney and Hartmann 1998; Riley et al. 2011). During boreal summer (June-September, JJAS), convection on this timescale tends to propagate northward into the Asian and West Pacific summer monsoon regions, and influence the onset of the monsoon in addition to producing active and break periods in the heart of the season (Wang and Xu 1997; Annamalai and Slingo 2001). This mode is often referred to as the boreal summer intraseasonal oscillation (BSISO).

While oceanic precipitation generally follows the enhanced moisture of the MJO active phase, several studies have shown a relative minimum in the amplitude of the diurnal cycle and in total precipitation over land masses during the active phase of the MJO (Sui and Lau 1992; Rauniyar and Walsh 2011; Oh et al. 2012). Such a signal has also been observed for regions impacted by the BSISO (e.g. Chen and Takahashi 1995; Ho et al. 2008; Xu and Rutledge 2018), although a weaker diurnal cycle is still present over land during the active phase (Chudler et al. 2020). Taking a more precise view, Peatman et al. (2014) demonstrated a peak in the amplitude of the diurnal cycle in the transition from suppressed to active MJO state for several MC islands using satellite observations. Vincent and Lane (2017) identified a double-peak in the diurnal cycle amplitude as a function of MJO phase in a WRF simulation, with a secondary peak at the end of the MJO active state, but noted this was less significant in observations.

The mechanisms involved in the MJO modulation of the diurnal cycle remain uncertain. Many of the above studies have attributed the enhanced diurnal cycle during the suppressed phase to the reduced cloudiness, which leads to a stronger thermal differential between the land and sea during daytime, and thus a stronger sea-breeze and stronger diurnal precipitation. This, however, would not explain the specific preference for a diurnal cycle peak near the end of the MJO suppressed period. Peatman et al. (2014) speculated that frictional moisture convergence associated with the Kelvin wave east of enhanced MJO convection (Gill 1980) can explain this difference. Equatorial wave dynamics fall short of explaining why the strongest diurnal cycle occurs during the transition to BSISO active conditions in the northern Philippines, much further from the equator (Natoli and Maloney 2019). In studies of the larger MC and South China Sea (SCS) region, Lu et al. (2019) and Chen et al. (2019) found moisture convergence to be an important factor, but attributed it to convergence of MJO-scale moisture by the local land-sea breeze circulation. Others have also pointed to moisture availability as a primary control on the diurnal cycle (e.g. Vincent and Lane 2017). Natoli and Maloney (2019) hypothesized using observations and reanalysis that a combination of moderate insolation, sufficient moisture, and weak low-level wind favors a strong diurnal cycle, consistent with Sakaeda et al. (2020) and a WRF simulation of a single MJO event by Vincent and Lane (2016). These environmental conditions tend to occur simultaneously during the transition from suppressed to enhanced intraseasonal convection (Natoli and Maloney 2019), and can also explain the preference for strong diurnal cycles in certain phases of other modes of convective variability like equatorial Rossby waves and the quasi-biweekly oscillation (Sakaeda et al. 2020; Natoli and Maloney 2021).

Near the Philippines, the low-level wind lags moisture in an MJO life-cycle by 1/8 to 1/4 cycle, and this could be a primary factor explaining why the diurnal cycle is enhanced during the suppressed-to-active transition, but not the reverse (Natoli and Maloney 2019, 2021). Since MJO moisture leads the westerly wind burst (e.g. Maloney and Hartmann 1998), the suppressed-to-active transition exhibits sufficient moisture, but weak easterly winds, while the reverse has similar moisture and insolation anomalies, but strong westerly winds (Natoli and Maloney 2019). Shige et al. (2017) showed that periods of strong environmental flow induced heavy total precipitation, but a small diurnal amplitude in India and Myanmar, while the opposite was observed during weak flow. They argued that strong winds can prevent the buildup of a thermal differential between land and sea, and thus weaken the sea-breeze and convection forced by it. Short et al. (2019) used satellite wind measurements over ocean to identify a correlation between a stronger offshore wind component (or weaker onshore wind component) and the amplitude of the diurnal perturbation in wind. An idealized modeling study of a small tropical island by Wang and Sobel (2017) found that the maximum precipitation rates associated with the diurnal cycle occurred with no background wind. Increasing the background wind resulted in more mechanically forced precipitation, but a reduction in the strength of the diurnal cycle.

The background wind has also been shown to influence where on an individual island precipitation forms. For example, while exploring the variability of local precipitation related to the MJO, Qian (2020) noted a tendency for wet anomalies in both the diurnal cycle and daily mean precipitation to occur on the leeward side of large MC islands and mountain ranges. Virts et al. (2013) found that lightning activity is also enhanced on the leeward side of topography, indicative of strong convection. Recently, Riley Dellaripa et al. (2020) examined the diurnal cycle over the Philippines through a high-resolution simulation of a 2016 BSISO event and found that the active phase, associated with strong westerly winds, shifted precipitation to the east (leeward) side of Luzon when topography was removed.

Other studies have examined the influence of the background wind on offshore propagation of diurnally generated convection. Convection that initiates in the afternoon has been observed to propagate offshore in the same direction as the mean lower-tropospheric wind during the evening and overnight hours (Mori et al. 2004; Sakurai et al. 2005; Ichikawa and Yasunari 2006; Yanase et al. 2017; Ruppert and Zhang 2019). Recent field data from the Years of the Maritime Continent (YMC) campaign west of Sumatra Island has also addressed this issue. Examining data from the November-December 2015 pre-YMC campaign, Wu et al. (2017) indicated that a strong, westward-propagating diurnal cycle was observed consistently during low-level easterlies prior to the onset of an MJO westerly wind burst. After the onset of the strong westerlies, the amplitude of the diurnal cycle was reduced and offshore propagation to the west ceased. Yokoi et al. (2019) reached interesting conclusions by comparing the December 2017 field data to the pre-YMC campaign. They noted that during the 2017 campaign, offshore propagation of diurnally generated convection was only observed on about half of the days, while it was nearly ubiquitous in 2015. They noted that the presence of a strong El Niño event in 2015 favored consistent easterly (offshore) wind anomalies, while the La Niña background in 2017 led to much more frequent westerly (onshore) winds. Additionally, they noted that the cooling in the lower free-troposphere attributed to convectively generated gravity wave propagation on diurnal timescales (e.g. Love et al. 2011; Hassim et al. 2016; Yokoi et al. 2017) was present on most days, regardless of whether convection propagated offshore. They concluded that gravity wave destabilization of the offshore environment may not be a sufficient condition for offshore propagation, and instead highlighted an important role for the low-level background wind.

This study aims to isolate the impact of the background wind on the diurnal cycle of precipitation over large tropical islands in observations and an idealized model. The goal of this manuscript is to demonstrate that much of the variability in the diurnal cycle of precipitation over a tropical island, from its strength to the direction and consistency of offshore propagation, can be inferred from the large-scale background wind on a given day. We consider the background wind to be any wind variability on timescales longer than the diurnal cycle. The idealized simulations here are inspired by previous results focusing on Luzon Island during boreal summer (e.g. Natoli and Maloney 2019, 2021), but the conclusions are not meant to be exclusive to this island. Our results are also designed to be agnostic to the reasons for variability in the background wind, but we anticipate the conclusions of this study will facilitate a better understanding of the relationship between large-scale modes such as the MJO and the diurnal cycle. We will show that much of the variability in the diurnal cycle can be attributed to variability in the environmental background wind. In the next section, a summary of the observational datasets and methods used will be described, followed by a description of the idealized model used to test the diurnal cycle under varying background wind conditions. Section 3 includes a discussion of observational results in which composites of the diurnal cycle near Luzon island in the Philippines are created based on the background wind profile . Section 4 describes the model simulations forced with the background wind profiles described in Section 3, examining variability in land-sea-breeze strength and offshore propagation. Additionally, a series of sensitivity experiments that aim to improve understanding of the primary factors determining propagation direction are explored. Lastly, a summary of the main conclusions of this study is given in Section 5.

2. Data and Methods

a. Observations

Satellite observations and reanalysis are used for the period June-September (JJAS) 1998-2020 in this study to examine the diurnal cycle as a function of the background wind, as well as set up and verify our model experiments. Vertical profiles of wind, temperature, geopotential height, and moisture on 27 pressure levels ranging from 1000-hPa to 100-hPa from the 5th Generation Reanalysis by the European Centre for Medium-Range Weather Forecasting (ERA5) are employed at 0.25° spatial resolution and hourly temporal resolution (Copernicus Climate Change Service (C3S) 2017; Hersbach et al. 2020). ERA5 single-level fields of mean sea level pressure (MSLP) and 2-m temperature (T2m) are also used at the same resolution. Satellite-derived precipitation estimates come from version 1.0 of the bias-corrected Climate Prediction Center Morphing Technique (CMORPH; Joyce et al. 2004; Xie et al. 2017). CMORPH data is examined at 8-km by 8-km spatial resolution and 30-minute temporal resolution. Tropical cyclone (TC) track data from IBTrACS (Knapp et al. 2018, 2010) also provide context on the TC impact frequency in the observational results. Lastly, topography data from NOAA ETOPO2 (National Geophysical Data Center 2006) is included as a reference for the local geography.

b. Binning Method

In order to stratify the period of record by vertical wind profile, a localized index is created to best represent flow on the west side of Luzon Island in the northern Philippines. Vertical profiles of zonal wind are averaged across all hours of the day, and spatially inside box A (Figure 1a) to create a single profile per day. Results are qualitatively insensitive to changes in the size of the box (up to covering the entire Philippines). Only ocean points were included to avoid capturing interference from the high topography of Luzon. The choice to place the box on the west side was guided by the preference for westward propagation of diurnally generated convection in this region during JJAS (Ho et al. 2008; Natoli and Maloney 2019; Lee et al. 2021; Xu et al. 2021).

Next, the first EOF of the vertical profile of daily averaged zonal wind was calculated for the study period (JJAS, 1998-2020) from 1000-hPa to 200-hPa. The purpose of this EOF analysis is to simply and cleanly classify days according to the sign and magnitude of the zonal wind throughout the column. Data was first spatially averaged and then standardized about the JJAS mean and standard deviation for each vertical level. While there is some seasonality within the JJAS season, the full JJAS period is considered to be within the westerly monsoon season and thus the effects of the seasonal cycle are minor. On average, the monsoon in the Philippines begins in mid-May and lasts until late-September (Matsumoto et al. 2020). The structure of the first EOF, which explains 73.7% of the variance, is shown in Figure 1b retained in physical units by projecting the unprocessed data onto the standardized principal component (PC) time series. Fig. 1b is scaled according to one standard deviation of the PC. The primary mode of variability is characterized by deep westerly (or easterly, since the sign is arbitrary) flow that maximizes in the mid-troposphere, but with similar amplitude to 900 hPa. This structure and its corresponding PC time series is then used as a proxy for daily mean flow impinging on Luzon. While this is not the main subject of this study, the power spectrum for the PC is shown in Fig. 1c. Peaks above a theoretical red noise power spectrum with the same autocorrelation as the PC (Gilman et al. 1963) are apparent at roughly the Madden-Julian Oscillation timescale (e.g. 30-90 days), the quasi-biweekly oscillation

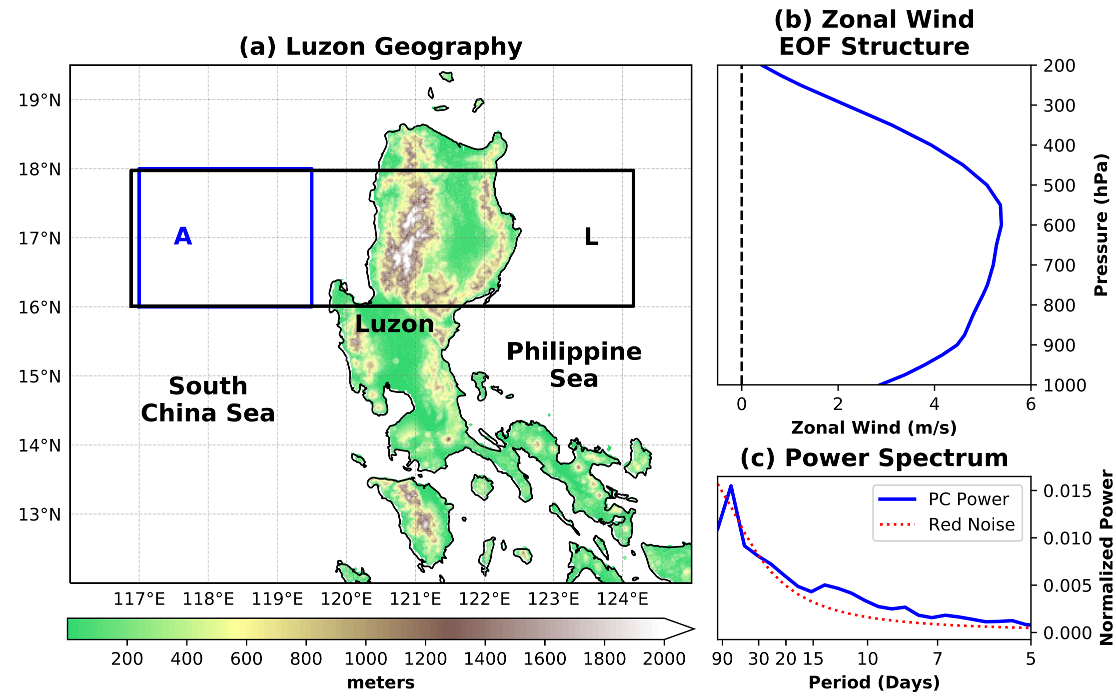

FIG. 1. (a) NOAA ETOPO2 Topography (in meters) over the northern Philippines, with boxes of spatial averaging and important geographic features noted. (b) Structure of the first EOF of ERA5 zonal wind averaged in JJAS 1979-2020 inside Box A of (a), in m/s, by pressure level (hPa). (c) Normalized power spectrum of the principal component (PC) time series corresponding to the EOF in (b) in blue, with a theoretical red noise spectrum based on a time series with the same autocorrelation as the PC time series shown in dotted red.

timescale (e.g. 10-15 days), and the synoptic timescale (e.g. less than 10 days), although none are statistically significant according to an F test at the 95% confidence level. However, this does highlight some variability in this index that may be modulated by various large-scale drivers.

Observational data is then binned by the Luzon zonal wind EOF index. Nine bins are selected, centered at 0.0σ, $\pm 0.5\sigma$, $\pm 1.0\sigma$, $\pm 1.5\sigma$, and $\pm 2.0\sigma$, where σ indicates the value of the PC time series on a given day. Each bin includes days with PC values within $\pm 0.25\sigma$ of the midpoint stated above, and are inclusive on the top end. The $\pm 2.0\sigma$ bins include days with PC values from $\pm 1.75\sigma$ to the minimum of -3.58σ or maximum of 3.92σ. ERA5 profiles of zonal wind, specific humidity, geopotential height, and temperature as well as the single-level values of MSLP and T2m are composited based on these bins. Additionally, a composite diurnal cycle of CMORPH data is generated for each of the nine bins, by averaging precipitation rates at the same times of day for all days in the bin. The number of days in each bin is indicated in Figure 2c, with the number of days in which a tropical cyclone (TC) center was located near Luzon (defined as inside 10-22°N and 115-127°E) also indicated. While the ±2.0σ bins were excluded from the observational analysis due to heavy TC influence, the TC days are still retained in the other bins. Removing them was tested and found not to qualitatively change the results.

c. CM1 Setup

Idealized experiments using version 20.2 of Cloud Model 1 (CM1; Bryan and Fritsch 2002) are performed to examine the sensitivity of the tropical diurnal cycle to the monsoonal background flow. One goal of this study is to realistically simulate aspects of the diurnal cycle in an idealized framework, which led to the decision to use CM1. This model has a fairly low computational cost and lends itself well to numerous sensitivity tests, some of which will be discussed in this manuscript, with work ongoing to analyze several others. The model is run in two-dimensions, with an 800-km domain in the x-direction at 1-km grid spacing, and a stretched vertical grid that begins at 50-m resolution in the boundary layer and increases to 1150-m at the domain top, which is at 20-km. This high-resolution allows for non-parameterized convection. A 2D framework aims to further simplify our analysis. This is suitable for qualitative comparison between model runs concerning convective initiation and propagation, but may fall short on quantitative aspects compared to reality (Rotunno et al. 1988; Grant and van den Heever 2016; Wang and Sobel 2017). Two of the simulations were examined in 3D and the conclusions were found to be unchanged. Another sensitivity test examined a higher model top and again found little change.

The parameterizations used include the Morrison double-moment microphysics scheme (Bryan and Morrison 2012), the NASA-Goddard radiation scheme adapted from the Advanced Regional Prediction System model, a revised surface scheme from WRF based on Monin-Obukhov similarity theory (Jiménez et al. 2012), and the Yonsei University planetary boundary layer scheme (Hong et al. 2006). The boundary conditions are open radiative at the lateral boundaries (Durran and Klemp 1983), partial-slip at the bottom, and free-slip at the top. The inflow boundary is nudged to the base state with a time scale of 60 seconds. A Rayleigh damping layer is applied above 15-km with an e-folding timescale of 300 seconds. In addition, a large-scale nudging technique

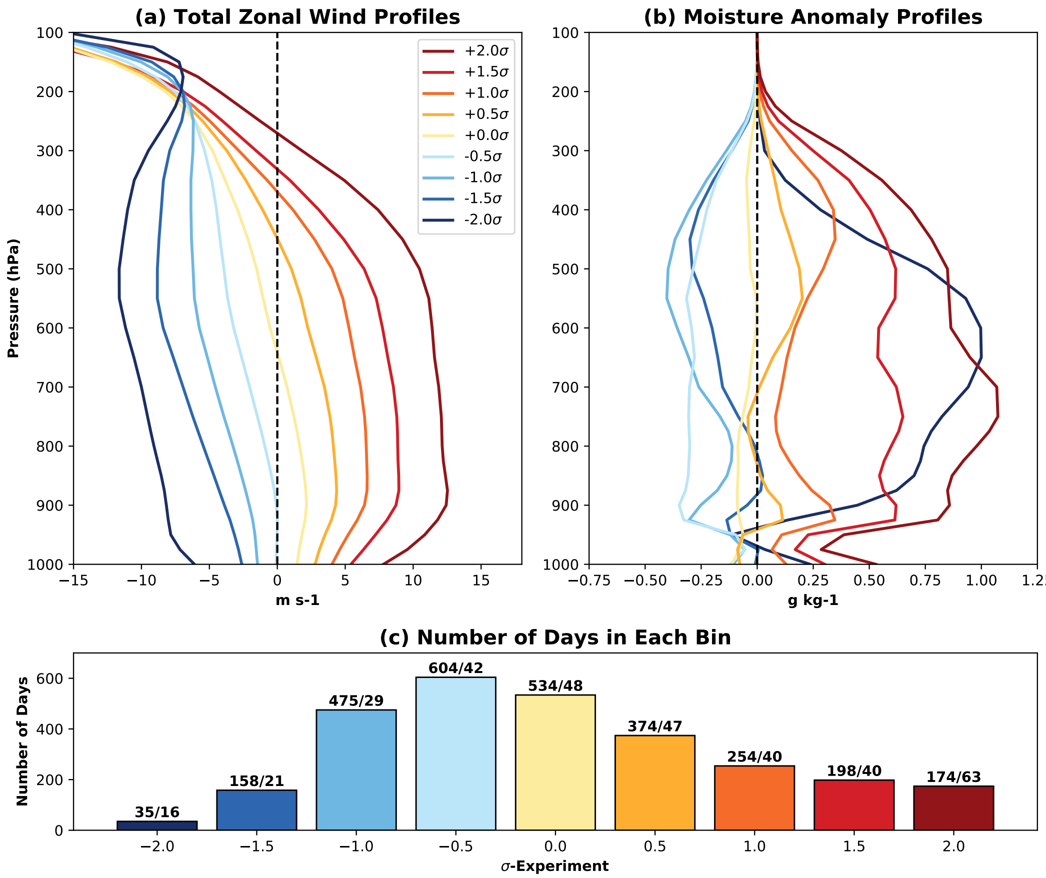

FIG. 2. (a) Composite ERA5 zonal wind profiles (m/s) for all JJAS 1998-2020 days that fall in a certain bin of the PC time series of the EOF in Fig. 1b. Values are averaged inside Box A (Fig. 1a). Bins include 0.25σ on either side of the value noted. That is, $+0.5\sigma$ days include any day between 0.25 and 0.75σ. The minimum and maximum bins are unbounded. (b) Anomalous moisture profiles in g/kg for the same bins noted in (a). (c) The number of JJAS 1998-2020 days that fall into each bin is shown as bars, with this number noted on top. The second number after the slash indicates the number of days in which a tropical cyclone center was near Luzon (inside 10-22N, 115-127E). Color coding is based on zonal wind, with easterly low-level wind bins shown in blues, and westerly bins shown in reds.

is implemented to the zonal wind, potential temperature, and water vapor mixing ratio to improve conservation and maintenance of the background wind. This term is applied uniformly across the domain at each time-step and vertical level, nudging the domain mean of each field back to the base-state with a timescale of 3 hours. Other timescales were tested, and 3 hours seemed to strike a good balance between maintaining base-state through the entire simulation, while also allowing the model to evolve its own diurnal cycle.

To simulate the coastal diurnal cycle, a 200-km island is placed at the center of the domain. This size is roughly the zonal extent of Luzon between 16-18°N. The model does not include topography, which is motivated by the results of Riley Dellaripa et al. (2020), who showed relatively minor differences in diurnal cycle behavior between runs with and without topography in their simulations of a BSISO event near Luzon. We acknowledge that lack of topography may affect interpretation of some of our results below, although we intend our results to be generalizable to a generic tropical island in the warm pool and not only Luzon. The land surface is defined as using parameters for a cropland/woodland mosaic land use, which again is representative of the lower elevations of Luzon. The base-state comes from ERA5. Initial surface temperatures come from the average SST inside Box A (Fig. 1a) for the ocean, and the average skin-temperature on land points below 400-m in elevation inside Box L. While the SST is fixed at the ERA5 mean value of 302.5K for all simulations, the soil temperature over land evolves freely, but does not systematically stray from its initial condition late in the simulation. This was the only SST value tested in this study, but exploring the sensitivity of the diurnal cycle in CM1 to the SST would be an interesting avenue for future research.

Initial surface conditions and the base-state sounding come from averages of the surface conditions and profiles in each of the bins of the zonal wind EOF index described in the prior section. This yields 9 different simulations, each with a different temperature, moisture, and wind profile (the latter two are shown in Fig. 2a-b), and different surface conditions. No initial perturbations are included, and the radiation is allowed to evolve the sea-breeze circulation and diurnal cycle naturally. The model is run with a solar cycle corresponding to 17°N, and initialized at 05:00 local time on 1 August (roughly the middle of the monsoon season for Luzon; Matsumoto et al. 2020). Each simulation is 14-days in length in order to capture internal day-to-day variability for each base state, and then diurnal composites are generated. Since the first day of the simulation was not substantially different from the later days, the spin-up time was determined to be short and all 14 days are retained in the subsequent analysis. Output is saved every 15 minutes. An additional set of 24 sensitivity tests was run for 7 days each with the same model configuration, with the goal of elucidating controls on the direction and speed of nocturnal offshore propagation. A detailed description of these experiments is left to Section 5, as presentation of the results from the main set of experiments is necessary to understand the motivation behind each set.

3. Observations

a. Daily Mean

Composites of CMORPH precipitation data based on bins of the zonal wind EOF index described above will be considered first to establish the importance of the background wind to the diurnal cycle in the real atmosphere and compare to prior studies near Luzon (e.g. Natoli and Maloney 2019, 2021). These results will be referenced in Section 4 to demonstrate that several realistic aspects of the diurnal cycle can be simulated in CM1. The average profiles in Box A (Fig. 1a) for each bin are shown in Fig. 2a-b. The bins well-stratify zonal wind, and are slightly skewed towards low level westerlies since the JJAS mean profile is westerly in the low levels (not shown). The more westerly bins tend to be moister than the easterly bins, consistent with the general behavior of monsoon season in the Philippines in which periods of moist, westerly monsoon activity are interspersed with drier easterly trade winds (Park et al. 2011; Chudler et al. 2020). One exception is the -2.0σ bin, which is from a very small sample of 35 days (Fig. 2c), nearly half of which had a tropical cyclone storm center near Luzon. The significant tropical cyclone influence explains why its corresponding humidity profile is much moister than average. Due to the small sample size, this bin is excluded from the observational discussion below. The results from the +2.0σ bin are generally a more extreme depiction of the results from the +1.5σ bin, and are also excluded from the discussion below for the sake of brevity. Both bins are retained for the model experiments to test more extreme conditions.

The CMORPH daily mean precipitation rate during JJAS is shown in Figure 3a, indicating high precipitation rates in excess of 10 mm/day over much of Luzon and the coastal SCS. The differences between the JJAS mean and the mean precipitation rate for each wind bin are shown in Figure 4. Statistical significance at the 95% confidence is shown as dots. This was calculated via a bootstrap method in which each composite was compared to the daily mean precipitation rate from 1000 random composites with the same number of days as each bin shown in Fig. 2c. Days

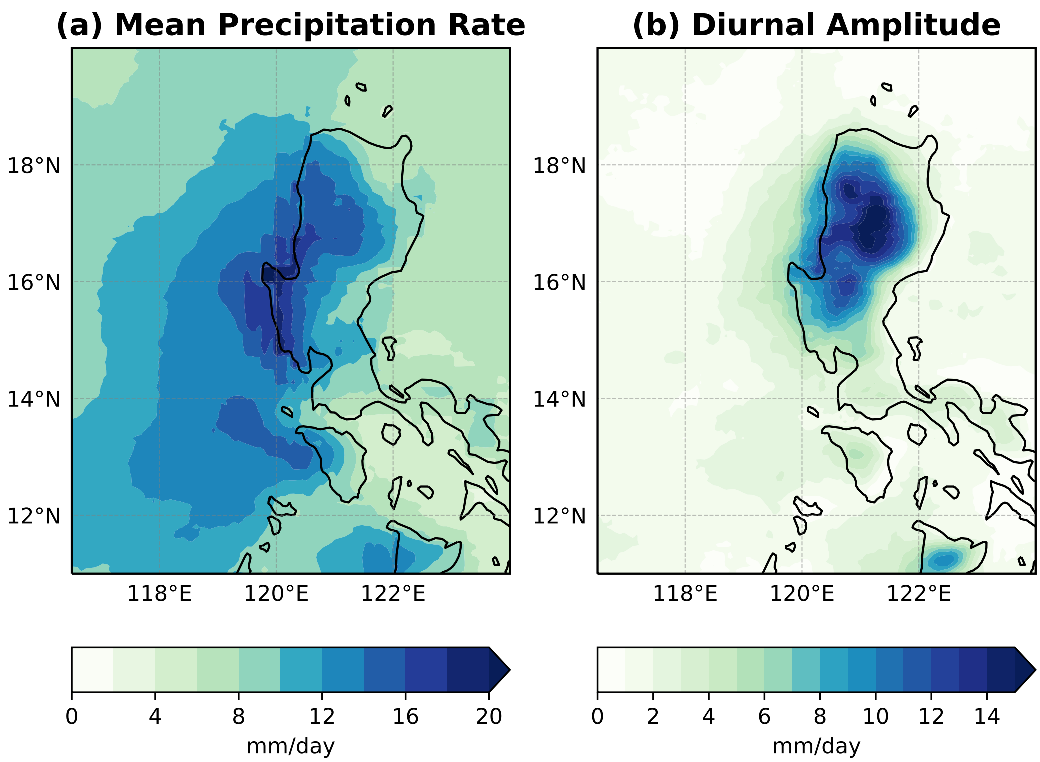

FIG. 3. (a) Daily mean precipitation rate (mm/day) from CMORPH (JJAS, 1998-2020). (b) Amplitude (mm/day) of the first harmonic of the JJAS CMORPH precipitation rate composite diurnal cycle.

with stronger westerly winds (e.g. +1.5, +1.0σ) experience elevated precipitation over the SCS, windward of the highest topography of Luzon. Similarly, the strongest easterly bins tend to exhibit reduced precipitation on the west (leeward) side of the island, but enhanced precipitation on the east (windward) side. Some counter-intuitive features are apparent in the middle three bins. For example, there is elevated precipitation on the east side of Luzon in the +0.5σ bin despite being on the leeward side of the island. As will be detailed in the next subsection, this may be explained by variability in the diurnal cycle that is enhanced on the leeward side of topography (Virts et al. 2013; Natoli and Maloney 2019, 2021; Qian 2020). This effect can be substantial enough to dominate the daily mean precipitation anomalies when the background wind is light.

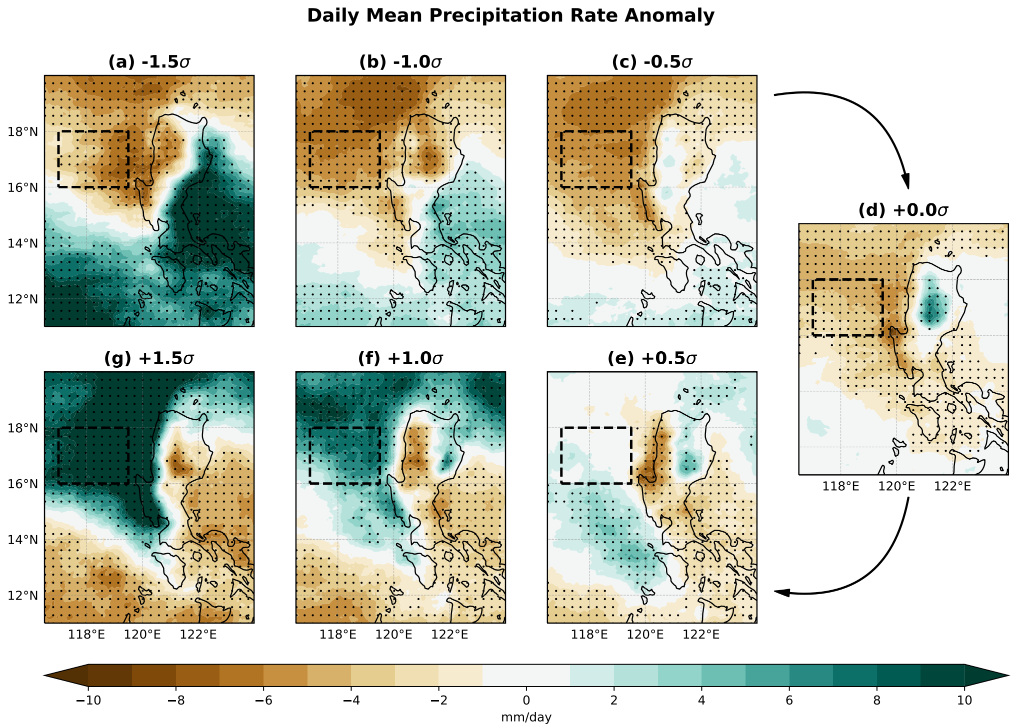

FIG. 4. Daily mean precipitation anomaly (mm/day) from CMORPH (JJAS, 1998-2020) averaged by bins of zonal wind EOF index. Anomalies are from the average precipitation rate on all JJAS days. Increasing zonal wind rotates clockwise around the figure. The +/- 2σ bins are not shown due to heavy tropical cyclone influence.

b. Diurnal Cycle

Many important aspects of diurnal precipitation variability in Luzon can be captured by compositing days according to the environmental wind alone. While the focus here is on the wind, ongoing research will attempt to address the relative importance of wind compared to other aspects of the environment that may co-vary with wind, such as moisture and insolation. In this study, the amplitude of the diurnal cycle is defined as the amplitude of the first harmonic of a composite diurnal cycle, as in Natoli and Maloney (2019). While there is some higher order variability, the first diurnal harmonic contributes about 60-90% of the intradiurnal variance over land and coastal waters as measured by the fit of the harmonic to the JJAS composite diurnal cycle. Thus, we will focus on this harmonic and ignore higher order modes for the purposes of this study. The diurnal amplitude of the JJAS composite diurnal cycle is shown in Figure 3b. Very high diurnal

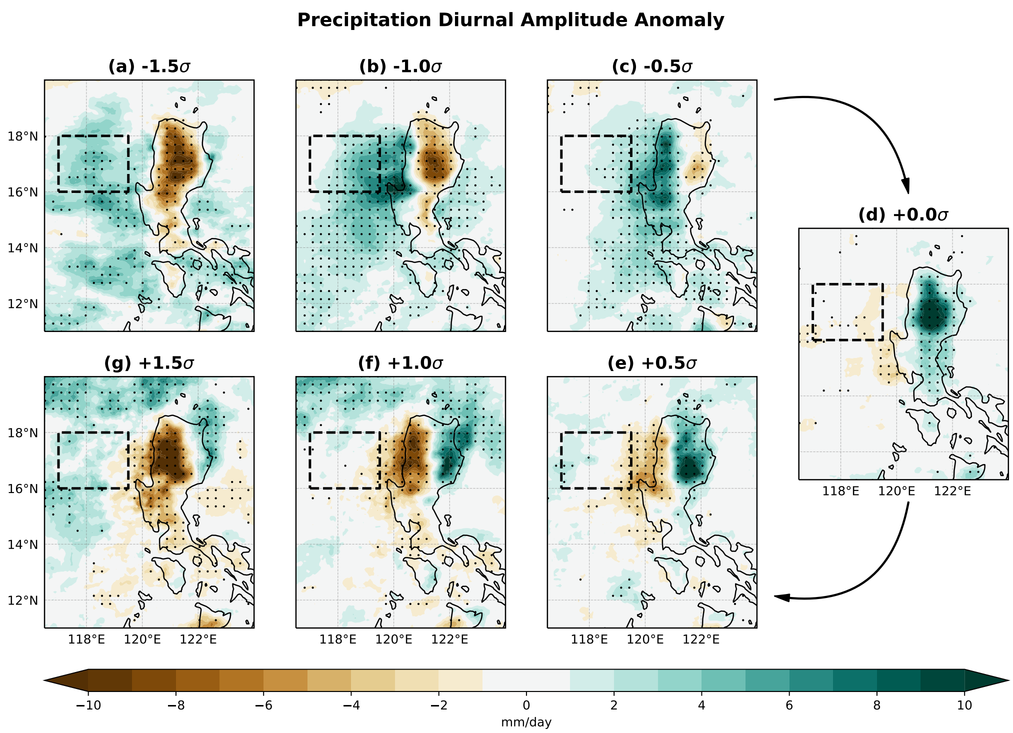

FIG. 5. Anomaly in the diurnal cycle amplitude (defined by the first harmonic of the composite diurnal cycle) composited by bin of the zonal wind EOF index for JJAS 1998-2020. Anomalies are from the amplitude of the full JJAS composite diurnal cycle. Increasing zonal wind rotates clockwise around the figure. The +/- 2σ bins are not shown due to heavy tropical cyclone influence.

amplitudes, exceeding the daily mean precipitation rate, are found over most of Luzon. The diurnal amplitude decreases to the west of Luzon.

Figure 5 shows the difference between the diurnal amplitude in the composite of days in each environmental wind bin, and the diurnal amplitude in the composite of all JJAS days. Statistical significance at the 95% level is again shown after the amplitude of the bin composite diurnal cycle is compared to the amplitude of the composite diurnal cycle in the 1000 random composites made for each bin. Details on the mean state of the boreal summer precipitation patterns near Luzon can be found in Natoli and Maloney (2019). The anomalies in diurnal amplitude binned by environmental wind alone are generally stronger over portions of Luzon than was found to be associated with large-scale modes like the BSISO (e.g. Figure 6 of Natoli and Maloney 2019).

Over land, the diurnal cycle is generally strong when the low-level zonal wind is weak (e.g. -0.5σ, 0.0σ, and +0.5σ bins), and weak when the low-level wind is strong (e.g. -1.5σ and +1.5σ), consistent with Shige et al. (2017). In addition, there is a noticeable preference for a strong diurnal cycle in the lee of the island. For example, days in the -1.0σ and -0.5σ bins (which have low-level easterly winds) tend to have a strong diurnal cycle on the west side of the island, and a weak diurnal cycle on the east side. The opposite behavior is apparent in the +1.0σ and +0.5σ composites. This is consistent with prior studies examining other MC islands with observations (e.g. Virts et al. 2013; Liang and Wang 2017; Qian 2020; Sakaeda et al. 2020). A clear shift is seen as westerly wind increases, starting with a weak diurnal cycle across all of Luzon during strong easterlies (e.g. -1.5σ), followed by a stronger diurnal cycle progressing across the island from west to east as weak to moderate easterlies transition to weak to moderate westerlies (e.g. -1.0σ to +1.0σ), leading to a strong suppression during strong westerlies (e.g. +1.5σ)

The offshore propagation of the diurnal cycle is also strongly associated with the vertical profile of zonal wind. Figure 6 shows Hovmöller diagrams of the composite diurnal cycle for each bin, latitudinally averaged from 16-18° in Box L (Fig. 1). The black line superimposed estimates the average propagation speed by finding a line of best fit between the longitudes of maximum precipitation rate at each 30-minute time step between 16:00 and 01:00 local time.

Fig. 6 clearly shows that while westward propagation of convection is prominent during the westerly monsoon season (e.g. Aves and Johnson 2008), this occurs largely on days in which the wind is more easterly than average (e.g. -1.5σ, -1.0σ, and -0.5σ days). In fact, days with near average or westerly zonal wind exhibit little westward propagation, but do display some preference for eastward propagation. On strong easterly days (-1.5σ), a weak enhancement of precipitation occurs on the western coastline in the late afternoon, that then propagates offshore overnight. This behavior is more obvious on weak to moderate easterly days (-1.0 and -0.5σ), where heavy precipitation forms over the high topography during the late afternoon, and then migrates predominantly to the west during the evening and overnight, propagating at roughly 5-6 m/s. When the wind is near the JJAS mean (0.0σ), strong precipitation is observed closer to the center of the island, with weak evening propagation in both directions. Observations in two field campaigns near Sumatra indicated similar dependence of offshore diurnal propagation on the wind profile normal to the coastline (Yokoi et al. 2017, 2019). While the timing is difficult to ascertain

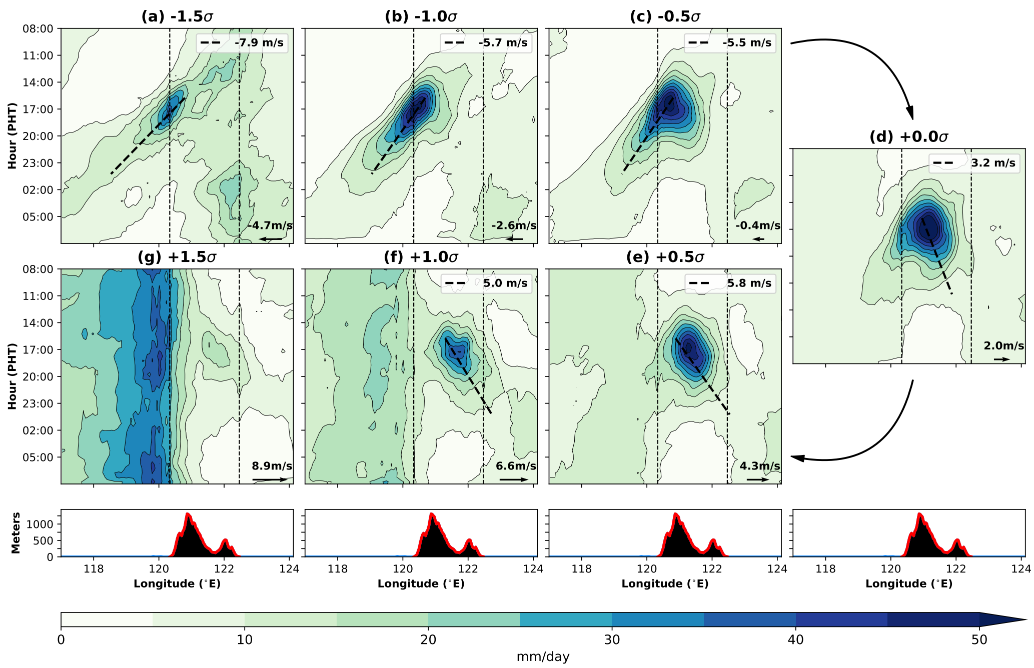

Fig. 6. Hovmöller diagrams of CMORPH composite precipitation rate (mm/day) on days binned by zonal wind EOF index averaged across latitude inside Box L (Fig. 1a). Time starts at 08:00 local time in each panel, and increases downward. dashed lines are estimates for a line of best fit between 16:00 and 01:00 of the longitude with the maximum precipitation rate at each time. This calculation only includes longitudes on the side of the island (east or west) that contains the maximum precipitation rate at 16:00. The estimated speed of propagation following this line of best fit is noted in the legend for each panel. This is not shown for the +1.5σ bin since little offshore propagation can be discerned. Increasing zonal wind rotates clockwise around the figure, with the composite 850-hPa zonal wind shown as a vector in each panel. The +/- 2σ bins are not shown due to heavy tropical cyclone influence.

from Fig. 6, closer analysis (not shown) indicates that the precipitation rate over land peaks about 30 minutes to one hour earlier on easterly wind days compared to moderate westerly wind days. This difference is subtle, but consistent with prior studies showing an later precipitation peak in the presence of onshore wind (e.g. Zhong and Takle 1993; Chen et al. 2017).

The westward branch disappears in weak to moderate westerlies (+0.5 and +1.0σ). Precipitation develops over the east side of the highest topography (near the center of the island), and then propagates to the east in the evening at roughly 5-6 m/s. However, convection moving to the east on these days does not tend to last as long or propagate as far when compared to westward propagating convection in the -1.0σ and -0.5σ bins. We speculate this may be due to the secondary mountain range on the eastern coast interfering with land-breeze and cold pool propagation, but this is beyond the scope of this study and could be a caveat of the modeling results below. During strong westerlies (+1.5σ), little precipitation is observed over the central and eastern part of Luzon, but very heavy rainfall is apparent over the SCS and western slope of the highest mountains throughout the day. These results are consistent with Ho et al. (2008), who also examined the Philippines, and an analysis of Sumatra island by Yanase et al. (2017). This behavior is also consistent with what many prior studies have shown regarding the relationship between large-scale modes of variability like the MJO (which impacts the wind profile) and the local diurnal cycle (e.g. Ichikawa and Yasunari 2006, 2008; Vincent and Lane 2016; Wu et al. 2017; Natoli and Maloney 2021). These observational results will be used as a benchmark against which to evaluate the successive model experiments.

4. CM1 Experiments

The CM1 simulations will be described in detail in this section. First, the general behavior of precipitation in each experiment will be discussed. Then in Section 4b, the sea-breeze circulation will be explored in more detail in order to explain why the diurnal cycle is stronger in the weak wind simulations. Section 4c will evaluate the extent to which gravity waves are important for determining the existence and speed of offshore propagation. Lastly, this section will conclude with a discussion of the sensitivity experiments that are designed to elucidate more information about the controls on propagation direction in the model.

a. Simulation Overview

Figure 7 shows the modeled precipitation rate for the full 14-days of the CM1 simulations (showing every other experiment for brevity). Precipitation develops nearly every day in all simulations, and relatively consistent behavior is seen from one day to the next. Notably, convection that develops over land (marked by the vertical dashed lines) propagates in the same direction on every day in the same simulation. This justifies our use of a composite of all 14 days for

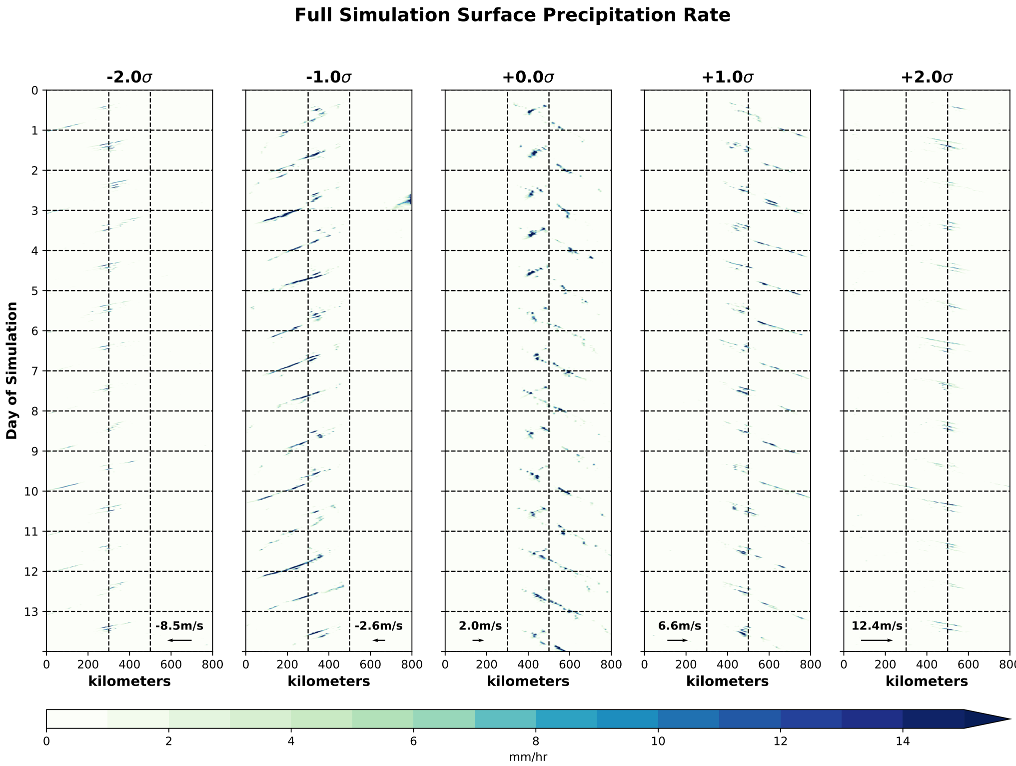

FIG. 7. Precipitation rate (mm/hr) for the full 14-day simulation of every other Cloud Model 1 (CM1) experiments. The x-axis in each is in km, with the coastlines marked as vertical dashed black lines. 05:00 on each day is noted as a horizontal dashed black line. The base-state 850-hPa zonal wind is shown as a labelled vector in each panel.

the remainder of this study, as some internal day-to-day variability in the diurnal cycle may be smoothed over, while highlighting signals present every day. Figure 8 shows the daily composite surface precipitation rate, found by averaging across all 14-days for every time step (i.e. 96 time steps at 15 minute intervals). For experiments that exhibit coherent offshore propagation, the best fit line connecting the longitude of maximum smoothed (to a 5-km grid) precipitation rate at each time step between 20:00 and 08:00 local time is shown as a dashed black line with its average propagation speed noted in the panel legend.

Remarkably, the idealized 2D simulation can capture several important aspects of the diurnal cycle in observations shown in Fig. 6. The easterly experiments (e.g. -1.5σ, -1.0σ, -0.5σ)

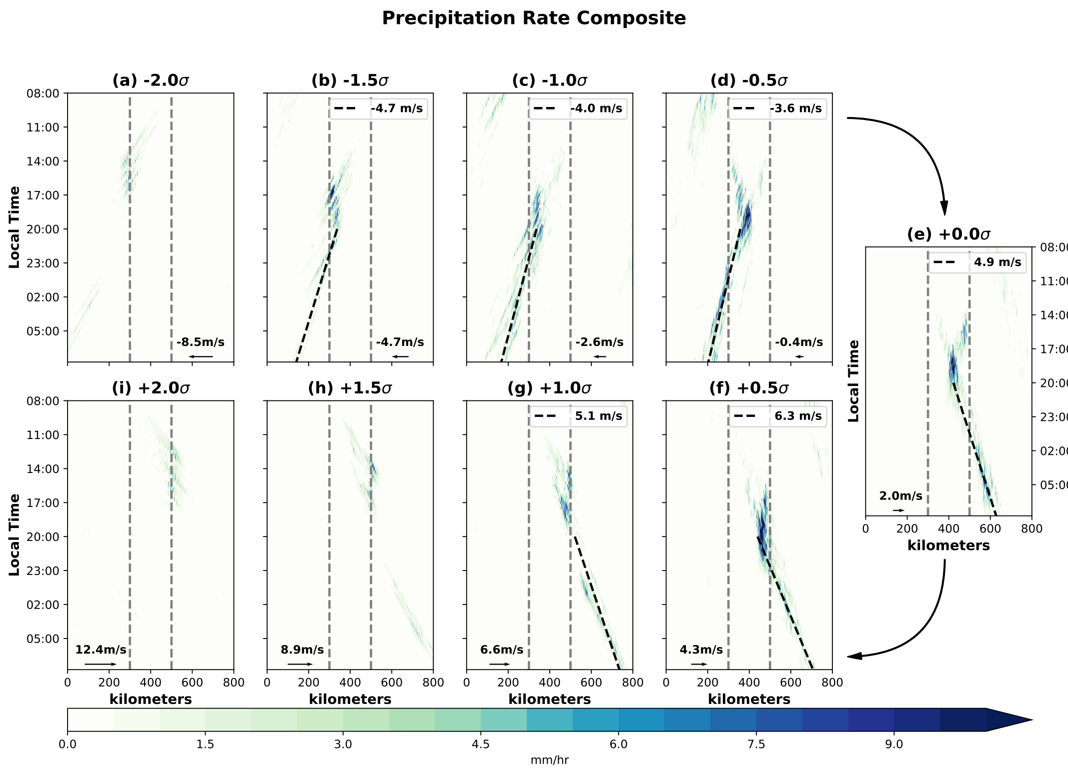

FIG. 8. Daily composite of the 14-day CM1 simulations showing precipitation rate by longitude at 1-km resolution. Each simulation varies the base state with the wind and moisture profile bins shown in Fig. 2 (as well as surface variables and thermal profiles, which are not shown). Dashed gray lines note the coastlines, and the dashed black line follows a line of best fit connecting the longitude of maximum precipitation rate at each time between 20:00 and 08:00. This is calculated based on precipitation rate smoothed to 8-km resolution. Increasing zonal wind in the base state rotates clockwise around the figure, with the base-state 850-hPa zonal wind shown as a labelled vector in each panel.

demonstrate mainly westward propagation, consistent with CMORPH observations. Similarly, the weak to moderate westerly experiments (e.g. +0.0σ, +0.5σ, +1.0σ) all exhibit eastward nocturnal propagation. The model propagates convection offshore at around 4-7 m/s, with some variability between the experiments. These speeds are consistent with land-breeze or cold pool propagation speeds (Finkele 1998; Vincent and Lane 2016; Hassim et al. 2016). The easterly experiments tend to initiate deep convection in the late afternoon over the west (leeward) side of the island, as in observations. The opposite is evident in the westerly experiments. These results complement prior modeling studies showing similar diurnal cycle behavior (Saito et al. 2001; Liang et al. 2017). Very strong background winds (e.g. the $\pm 2.0\sigma$ experiments) suppress the diurnal cycle, as was also seen in observations. Since most of the modeled precipitation comes from the diurnal cycle, convection is suppressed altogether in the strong background wind simulations. Precipitation tends to develop earlier in the day, reaches a weaker maximum, and dissipates faster in the strong wind experiments, consistent with other modeling studies (Zhong and Takle 1993; Chen et al. 2017; Wang and Sobel 2017).

Deep convection appears to develop closer to the eastern coastline in the $+0.5\sigma$ and $+1.0\sigma$ simulations than in the corresponding observations. In addition, storm longevity is symmetric between eastward and westward observations in the model, unlike observations, possibly because of the lack of topography in the model. This can be explained by invoking the results of Riley Dellaripa et al. (2020), who showed that the presence of topography in a simulated diurnal cycle over Luzon focused precipitation over the mountains in suppressed BSISO conditions (analogous to our easterly experiments). However, it is worth noting that Riley Dellaripa et al. (2020) found a relatively modest change in diurnal cycle behavior without topography, which was partial motivation for incorporating the simplification of flat topography in our simulations. The asymmetry in observations that is not present in the flat model may be explained by the concentration of the highest peaks near the western coast (Fig. 1) and the lower mountains near the east coast interfering with eastward propagation. Additionally, the flat topography may contribute to timing differences between the model and observations. The modeled precipitation rate over land (Fig. 8) peaks slightly later than in observations (Fig. 6). This is again consistent with the results of Riley Dellaripa et al. (2020), who showed that the presence of topography leads to an earlier diurnal cycle peak during suppressed MJO conditions, which would be roughly analogous to the weak wind simulations here where this timing difference is most evident.

b. Land-Sea-Breeze Circulation

Much of the variability in precipitation behavior over land during the day between background wind experiments can be attributed to the modulation of the strength of the sea-breeze circulation. While the discussion surrounding propagating sea-breeze fronts may not be directly applicable to our example case of Luzon due to the lack of topography in the model, this is still useful to understand the processes governing the model behavior. Figure 9 shows composite zonal wind at the lowest model level (25m) for every other simulation. The top row (a-e) shows the total wind, while the bottom row (f-j) shows the perturbation from the base state. In the simulations with a weaker wind speed (e.g. -1.0σ and 0.0σ, Fig. 9b-c, g-h), a roughly symmetric sea-breeze, indicated by an onshore wind, begins to develop around 08:00, and then expands offshore and propagates inland from both coastlines. The sea-breeze front can be identified as the transition zone from near zero perturbation zonal wind to anomalous onshore flow (i.e. westerly flow on the west coast or easterly flow on the east coast) over the landmass during the day. In the 0.0σ experiment, some weak precipitation is visible between about 11:00 and 17:00 along each sea-breeze front, but strong convection doesn't develop until the two sea-breeze fronts converge, at around 17:00 (Fig. 8). The asymmetry in which side of the island experiences stronger convection is also illustrated in the sea-breeze front. The sea-breeze front appears to propagate inland faster on the windward side (e.g. towards the lee), leading to initial convergence between the two fronts on the leeward side (e.g. Saito et al. 2001). In the strong wind experiments, the sea-breeze is much weaker, with little diurnal change in the wind on the windward side, and anomalous onshore flow in the afternoon on the leeward side that temporarily cancels the prevailing offshore flow (Fig. 9a,e,f,j).

The sea-breeze arises from a sea-to-land oriented pressure gradient force caused by differential heating between the land surface and the ocean with a much greater thermal inertia. While the general behavior of the low-level wind is shown in Fig. 9, Figure 10 shows the pressure gradients that would propel such behavior. The average perturbation pressure over land reaches a minimum around 15:00 and a maximum around 20:00 to 23:00. This leads to the maximum acceleration in the onshore low-level zonal wind during the mid afternoon hours (Fig. **??**). The pressure gradient is measured in Fig. 10b by the maximum difference between lowest model level pressure over land and over ocean on the leeward side in order to clearly extract the differences between simulations. As expected, the maximum pressure gradient occurs in the -0.5σ simulation, which has the weakest low level background wind (Fig. 2a). As the background wind increases in both the westerly and easterly directions, the pressure gradient decreases, leading to a weakening sea-breeze with stronger wind.

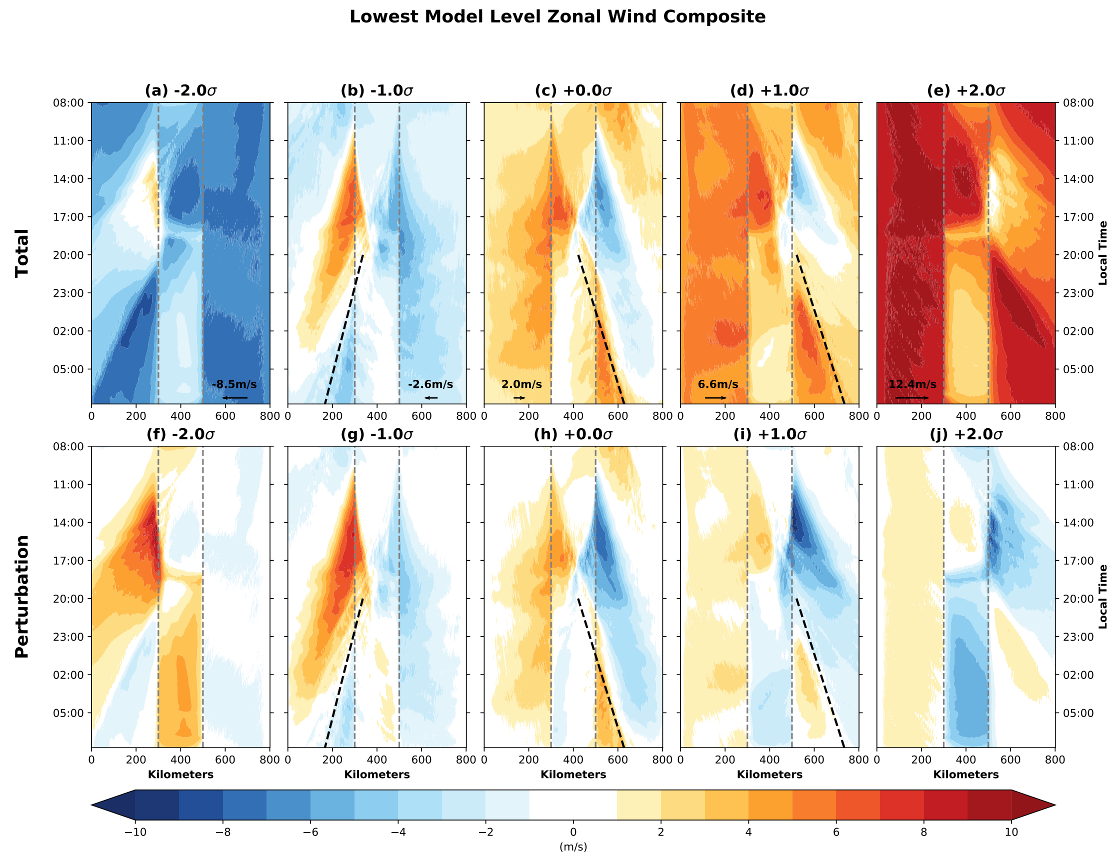

FIG. 9. Lowest model level zonal wind (in m/s) Hovmöller diagrams for every other experiments. The total zonal wind is shown on the top, and the perturbation from the base-state is shown on the bottom. The line of best fit for the maximum precipitation rate shown in Fig. 8 for the corresponding experiment is shown as a dashed black line. Coastlines are denoted with dashed gray lines. The base-state 850-hPa zonal wind is shown as a labelled vector in each panel in the top row.

Figure 11 demonstrates the impact of the prevailing wind on the thermal properties of the land surface and the onshore wind. Marked variability can be discerned depending on the background wind. On the western half of the island in the strong westerly experiments, the amplitude of the diagnosed 2-m temperature (T2m) perturbation is much smaller than in the weak to moderate easterly experiments (Fig. 11a). The +2.0σ simulation, for example, has a nocturnal minimum temperature of around 25.5°C, and a daily maximum of around 31°C. The -1.0σ experiment conversely drops to 24.5°C at night, and warms to nearly 34° during the day. Inverse behavior is

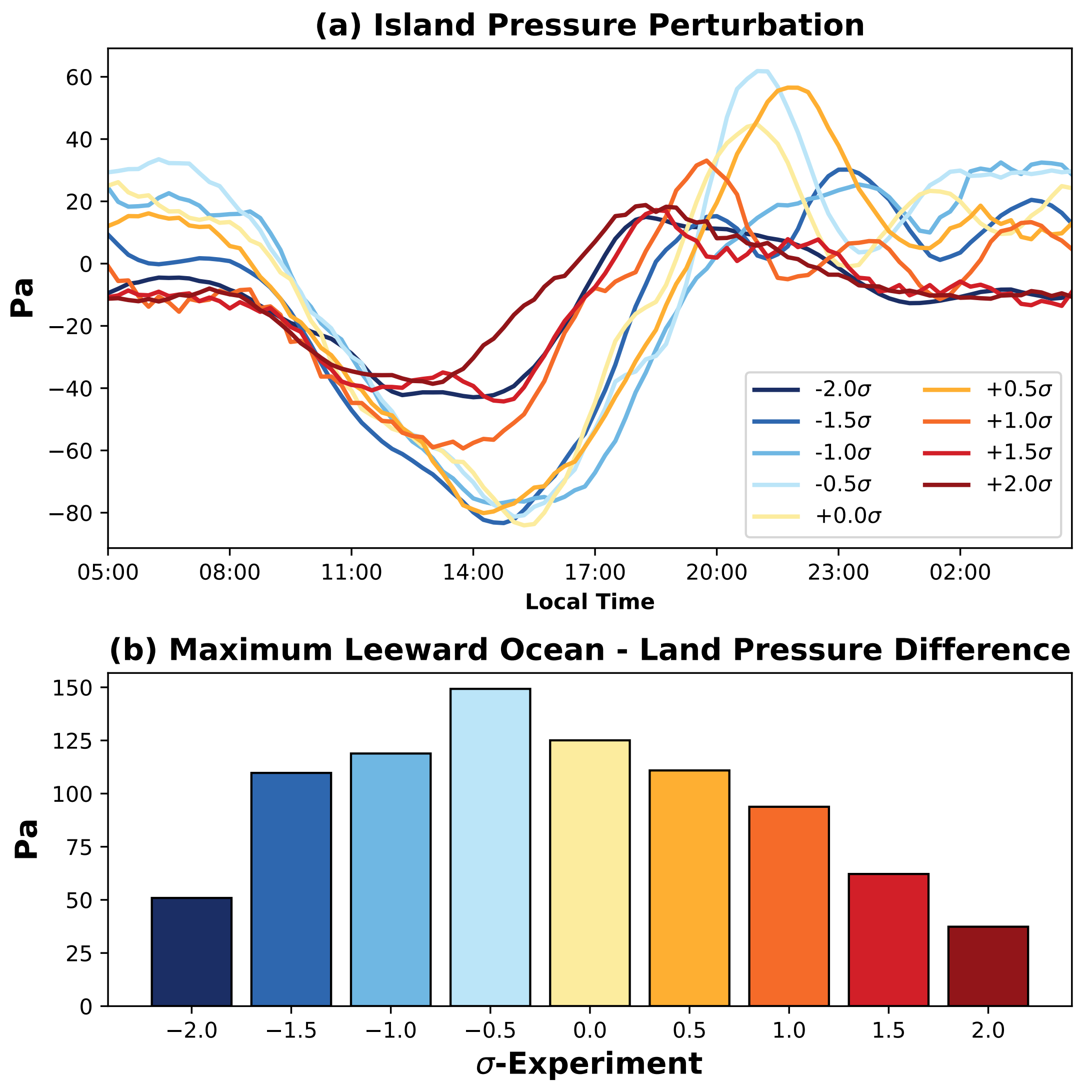

FIG. 10. (a) 14-Day composite perturbation pressure (in Pa) on the lowest model level averaged over the island and smoothed with a one-hour running mean for each of the experiments. (b) Maximum difference between average lowest model level pressure over the island and over the ocean on the leeward side in the composite (west side for -2.0 through -0.5σ experiments, east side for +0.0 through +2.0σ experiments).

seen over the eastern half of the island, with weak thermal contrast in -2.0σ and the strongest T2m diurnal cycle in 0.0σ (Fig. 11b). The strongest wind experiments reduce the afternoon maximum

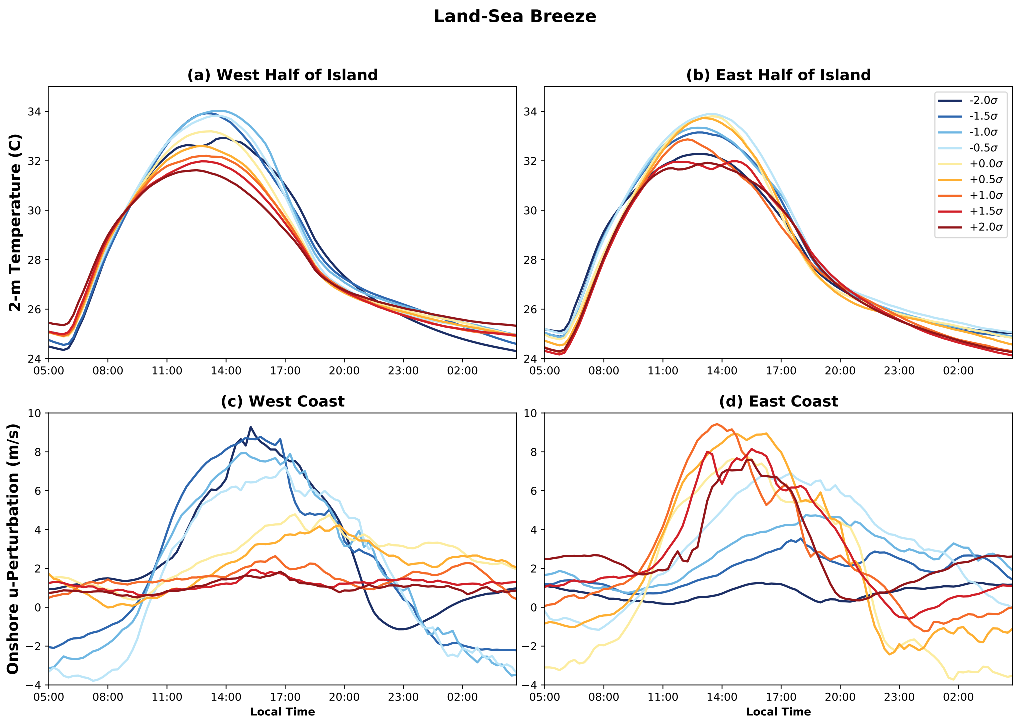

FIG. 11. (a) Diagnosed 2-m temperature (C) for each experiment averaged for each time across the western half of the island. (b) As in (a), except averaged over the eastern half of the island. (c) Onshore (i.e. westerly positive) perturbation zonal wind (m/s) at the lowest model level (25m) for each experiment averaged for each time between the western coast and 25-km offshore. (d) As in (c), except with easterly winds defined as positive, averaged between the eastern coast and 25-km offshore.

temperature even on the leeward side. This is more obvious on the west half of the island, likely due to the asymmetry in wind speeds through all simulations (e.g. the magnitude of the wind in the $+2.0\sigma$ experiment is greater than the -2.0σ experiment). Thus, the amplitude of the T2m diurnal cycle appears to maximize during weak to moderate offshore prevailing winds.

The alterations in surface thermal contrast also affect the coastal low-level wind (Fig. 11c-d). The onshore perturbation-u (u')is dramatically stronger on the leeward side on both coasts. u' is around 6-9 m/s during the afternoon hours on the leeward coast, but generally much weaker (0-5 m/s) with a peak later in the afternoon on the windward coast. These results support the hypotheses of many prior observational studies arguing that a strong prevailing wind can alter the diurnal cycle by ventilating the land surface, reducing the land-sea thermal contrast, and thus the sea-breeze circulation on the windward coast (e.g. Shige et al. 2017; Natoli and Maloney 2019, 2021; Qian 2020).

There are also substantial differences in nocturnal land-breeze behavior and the offshore propagation of precipitation. In Fig. 11, onshore prevailing wind leads to essentially no development of a land-breeze on the windward coast, as indicated by the lack of onshore perturbation-u below zero in the 0.0σ through +2.0σ experiments on the west coast (Fig. 11c) and in the -2.0σ through -0.5σ experiments on the east coast (Fig. 11d). On the lee-side, weak offshore flow develops in the late evening, supporting enhanced convergence and thus nocturnal precipitation. It is worth noting when considering Figs. 9 and 11 together that the spatial average in Fig. 11c-d only includes ocean points within 25-km of the coast. In Fig. 9, the land-breeze is identified by the development of an offshore wind on the leeward coast (e.g. easterly wind on the west coast in the -1.0σ experiment, and westerly wind on the east coast in the 0.0σ and +1.0σ experiments), that then propagates offshore in the leeward direction with precipitation. In the weak wind experiments (Fig. 9g,h,i), a land-breeze develops around 20:00. The composite precipitation signal propagating offshore (Fig. 8 and dashed line in Fig. 9) generally follows the maximum convergence associated with the land-breeze front (not shown), which can be inferred from the gradient of low-level zonal wind overnight in Fig. 9. Interestingly, the strong wind experiments exhibit nocturnal leeward propagation of low-level offshore winds that are stronger than the background wind (i.e. negative perturbation moving westward overnight in Fig. 9f and positive perturbation moving eastward overnight in Fig. 9j). This signal is mostly uncoupled from convection, although precipitation does form on this boundary on a few days in the simulation (Fig. 7a). We speculate that this is related to the timing of precipitation. Convection has already largely dissipated in the strong wind experiments by the time the land-breeze initiates. While it is possible that the apparent land-breeze in the weak wind simulations (Fig. 9g,h,i) is simply the low-level wind contributed by the outward spread of rain-cooled air in the convective cold pool, the fact that a similar signal appears in the strong wind experiments in the absence of convection allows for a hypothesis regarding the causal direction. This behavior seems to indicate that the land-breeze zonal wind signal is driving precipitation in these simulations rather than the other way around.

The relationship between the offshore propagation of precipitation and convectively generated gravity waves was also explored. Gravity waves have frequently been shown to be important for the propagation of diurnally generated tropical convection (Grant et al. 2018), either through direct coupling of convection to propagating gravity waves (e.g. Mapes et al. 2003; Lane and Zhang 2011), or by destabilizing the offshore environment in advance of convection propagating with the land breeze or cold pool (e.g. Love et al. 2011; Hassim et al. 2016; Yokoi et al. 2017; Vincent and Lane 2018). While gravity waves of multiple orders that likely develop in response to different convective heating profiles are apparent in these simulations, offshore propagation cannot be convincingly tied to any one gravity wave mode. However, there is evidence of destabilization of the offshore environment in advance of offshore propagation convection that could be related to gravity waves.

Figure 12 shows the 14-day composite convective available potential energy (CAPE), convective inhibition (CIN), and the level of free convection (LFC) averaged across the nearest 100-km of coastal waters on the eastern side of the island in the 0.0σ simulation. The offshore environment is most stable around 16:00, as indicated by a minimum in CAPE and maximum in CIN and the LFC. The environment then gradually destabilizes through the evening hours, with instability peaking after midnight as precipitation starts to ramp up offshore. The late afternoon and evening destabilization time period corresponds to the peak and decay of land-based precipitation. Further analysis of the potential temperature budget (not-shown) leads to speculation that gravity waves initiated by different diabatic heating profiles relating to convection could contribute some of this destabilization. However, establishing this conclusively is beyond the scope of this paper. Further analysis of the gravity wave behavior in these simulations can be found in (Natoli 2022).

To summarize, a stronger background wind in our simulations leads to a reduction in the thermal differential between land and water (Fig. 11a, b), which then leads to a reduced land-sea pressure gradient (Fig. 10b), and produces a weaker land-sea breeze circulation especially on the windward coast (Figs. 9 and 11c,d). The sea breeze fronts propagate inland from both shores with weak to moderate wind, but tend to converge and initiate convection on the leeward side of the island due to the windward front propagating faster. A signal resembling a land breeze can be seen propagating off the leeward coast in all simulations, but this has a stronger coupling to precipitation in the weaker wind simulations. These results add support to the hypothesis that surges of the monsoon lead to

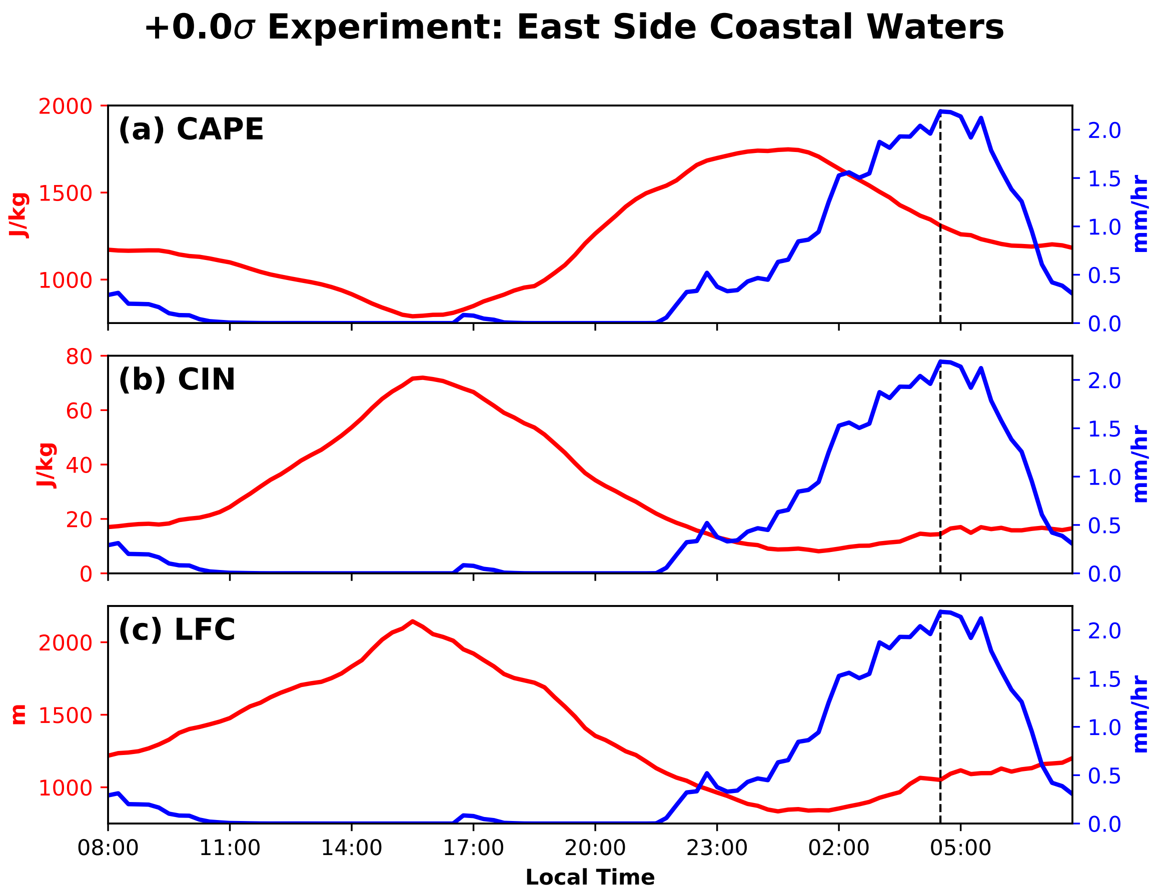

FIG. 12. 14-day composite CAPE (a; J/kg), CIN (b; J/kg), and LFC (c; m) averaged across the nearest 100-km of coastal waters on the eastern side of the simulated island in red, with composite precipitation rate (mm/hr) averaged in the same region in blue.

a reduced land-sea temperature contrast, and thus a weaker sea-breeze and precipitation diurnal cycle. Offshore propagation in these simulations appears to be driven by low-level convergence associated with the land-breeze, with a potential contribution by gravity waves towards offshore destabilization, consistent with (Bai et al. 2021).

c. Direction of Propagation Sensitivity Experiments

In this section, the sensitivity of the direction of precipitation propagation to the details of the zonal wind profile will be considered. Fig. 8 shows that modeled precipitation exhibits clear westward propagation in -0.5σ, but clear eastward propagation in 0.0σ. There is still a fairly large gap between these two wind profiles, particularly considering the depth of the low-level westerlies (Fig. 2). Weak easterlies cover the entire profile in the -0.5σ base-state, while weak westerlies reach up to nearly 600-hPa in the 0.0σ base-state. Thus, additional sensitivity experiments were designed to fill in these gaps, while also testing the response to different low-level shear profiles. These experiments were divided into three sets of 8 each, run for 7 days with the moisture and thermodynamics of the 0.0σ experiment, but with adjustments made to the vertical structure of the zonal wind profile to assess the importance of flow at different levels diurnal precipitation behavior.

Specifically, Experiment Set 1 will fill in the gaps between the -0.5σ and 0.0σ experiments to see how deep low level westerly flow needs to be to initiate eastward propagation of precipitation. Experiment Set 2 tests whether a narrow layer of westerlies in the lower free troposphere can lead to eastward propagation under constant low-level westerly shear. Finally, Experiment Set 3 tests if a different depth of the westerly layer is required to initiate eastward propagation when under constant low level easterly shear. The results in this section will show that, at least in these CM1 simulations, the zonal wind in the lower free troposphere appears to be the primary factor determining whether convection will propagate to the east or the west, while the boundary layer wind determines which side of the island diurnal precipitation will develop on before propagating in one direction or the other. The differences between each experiment set are displayed graphically in Figure 13.

Some prior papers on tropical squall lines have broached similar subjects, and will be briefly discussed here. Observations by Keenan and Carbone (1992) indicated that monsoon-break season squall lines appeared to propagate in the direction of the 700-hPa winds. Peters and Hohenegger (2017) noted that convection initially propagates in the direction of the background wind (vertically unidirectional in their experiments). Others have implicated the wind shear as an important factor determining convective organization and propagation direction (e.g. Rotunno et al. 1988; Nicholls et al. 1988; Liu and Moncrieff 1996; Tulich and Kiladis 2012). Tropical squall lines may also act to reduce the wind shear through vertical mixing which homogenizes the zonal wind profile (LeMone et al. 1984). However, the shear profile used in the experiments discussed so far not as strong as that used in most of these studies, so other processes may be more important for determining propagation direction in this environment (Grant et al. 2020). These ideas will be relevant to the discussion of the next several figures.

Figure 13 shows the base-state zonal wind profiles for each of the sensitivity tests described in this section. The color coding for each line indicates the propagation velocity, where red is eastward propagation and blue is westward propagation. The gray profiles either had visible propagation in both directions, or unclear propagation that caused the objective algorithm to fail. The first set (Fig. 13a) labeled Exp. 1.1 through 1.8 is simply a linear interpolation between the -0.5σ and 0.0σ simulations (where 1.1 is identical to the -0.5σ experiment and 1.8 is identical to the $+0.0\sigma$ experiment). Set 1 shows that once westerlies extend to a depth of about 800-hPa or deeper in CM1, precipitation will propagate eastward.

The idea for set 2 (labeled Exp. 2.1 through 2.8) stemmed from these results, and aims to address whether a layer of westerlies centered in the lower free troposphere could lead to westward propagation when the surface winds are easterly also. To accomplish this, a new profile was created in which the low-level winds of set 1 are modified. If the set 1 profile is more westerly than extrapolation of a line connecting a 1000-hPa wind of -1 m/s and an 900-hPa wind of 0 m/s the wind is set to the value of the extrapolated line instead (Fig. 13b). When the westerly layer is thicker than about 150-hPa (as in Exps. 2.5 to 2.8), eastward propagation ensues despite the easterlies below 900-hPa. We then wanted to address the role of the boundary layer shear, which inspired set 3 (labelled Exp. 3.1 to 3.8). This is done by extending the average shear between 800-hPa and 850-hPa of the original profile (interpolated between the -1.0σ and 0.0σ) to the surface (Fig. 13c). The propagation direction in each of these shows relatively similar results to set 1. Once the westerlies extend deeper than about 800-hPa (Exps. 3.6 through 3.8), precipitation starts to propagate eastward despite the easterly shear. This indicates that the depth of the westerlies is likely more important than the shear included at the magnitude in this study.

These sensitivity tests can also address some questions regarding the speed of propagation. In all of these experiments, the propagation speed is generally between 3 and 5 m/s in either direction, although the environmental wind is only greater than 3 m/s below 600-hPa in a handful (easterly winds in Exps. 3.1 through 3.4). Westerly environmental winds of greater than 3 m/s are found nowhere in any profile. Thus, it is unlikely that the precipitation propagation seen in the model is simply advection by the wind. Rather, these are propagating disturbances that move faster than the environmental wind (Lafore and Moncrieff 1989).

****** Cold Pool Speeds **********

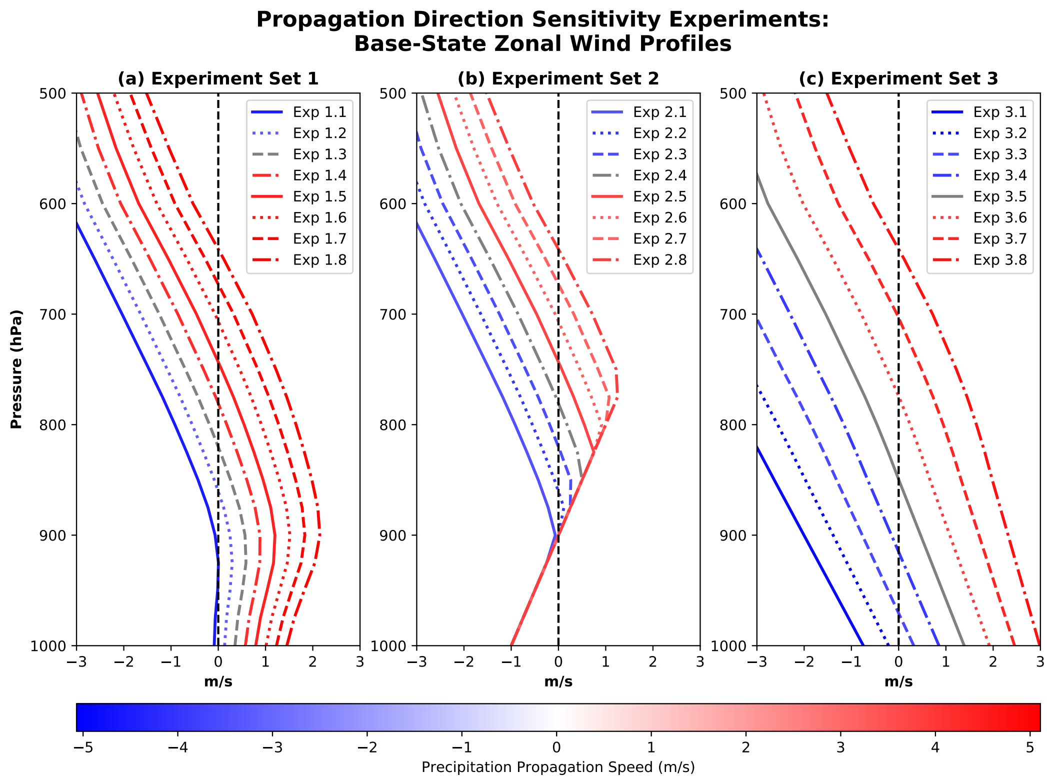

FIG. 13. (a) Idealized base-state zonal wind profiles in the lower troposphere for sensitivity experiments set 1, based on linear interpolation between the -0.5σ and +0.0σ experiments shown in Fig. 2a. (b) As in (a) but for sensitivity experiments set 2, which are taken from set 1, but forced to a line (in pressure-wind coordinates) connecting a wind of -1 m/s at 1000-hPa and 0 m/s at 900-hPa if the set 1 profile is more westerly than the ideal line profile at a given height. (c) As in (a) but for sensitivity experiments set 3, which are interpolated between the -1.0σ and 0.0σ experiments, with the shear profile between 800-hPa and 850-hPa extended to the surface. Profiles are color coded by the propagation velocity of the smoothed (to 5-km spacing) maximum precipitation rate between 20:00 and 08:00 in each experiment, with red indicating eastward propagation, and blue indicating westward propagation. The gray profiles are chosen subjectively as experiments with weak or inconsistent offshore propagation in which the objective algorithm to calculate propagation speed failed.

Figure 14 shows the zonal wind averaged within 25-km of the smoothed precipitation maximum between 17:00 and 20:00. Eastward propagating experiments have fairly well-mixed westerly winds between 900-hPa and 700-hPa, with the converse in the westward propagating experiments. The vertical profile in the lower free troposphere is much more homogeneous in these profiles compared to the base-state profile (Fig. 13), indicating that convection could be mixing horizontal momentum vertically (e.g. LeMone et al. 1984). During the convective maximum, the vertical wind shear is greatly reduced, and the resulting more uniform vertical wind profiles are generally quite consistent with the direction (but not speed) of offshore propagation. This leads to the hypothesis that the propagation direction is determined by the average base-state momentum through roughly the 700-hPa to 900-hPa layer which is mixed and homogenized by convection. It is unclear why the mixing does not appear to extend to the PBL below 900-hPa in these simulations, since Fig. 14 still shows some substantial shear in the lowest levels.

While the flow in the lower free-troposphere appears to be important for determining propagation direction, the PBL background flow is likely important for determining where within the island the heaviest precipitation falls. Figure 15 shows a scatter-plot of the average x-coordinate of maximum precipitation rate between 17:00 and 20:00 with the base-state wind at 0.68-km for each of the 24 sensitivity tests. This level yields the highest correlation coefficient of 0.97, which drops off to 0.84 when the lowest model level wind is used, and to 0.69 with the 1.98-km wind. The correlation coefficient of the location of maximum precipitation rate with the average wind in the roughly 700-900-hPa layer is 0.78. The mechanism involved here appears to be that the PBL background flow modifies the speed of the sea-breeze fronts, and leads to their convergence on the leeward side of the island. This behavior can be seen in Fig. 9 for the main set of experiments in this study, in which the afternoon sea-breezes on each side of the island converge on the leeward side. For example, in the -1.0σ experiment (Fig. 9b,g), the easterly sea-breeze propagates further inland than the westerly sea-breeze on the west (leeward) coast, and the convergence and precipitation maximum occurs on the west side of the island (Fig. 8b). When the wind is westerly as in the +1.0σ experiment (Fig. 9d,i) the sea-breeze fronts converge on the east (leeward) side of the island.

The variability in the location of maximum precipitation rate in experiment Set 2 shows roughly the amount of random spread that could be expected, since all of these have the same low-level wind. Comparing these locations to the wind aloft (Fig. 13b) does not reveal any relationship between the location of maximum precipitation in set 2 and the wind higher in the atmosphere. This supports the idea that this is just what can be expected with random variability. An interesting observations from the set 2 experiments can be identified invoking some previous work. Carbone et al. (2000) proposed that the ideal condition for long-lived diurnally forced convection is a flow-

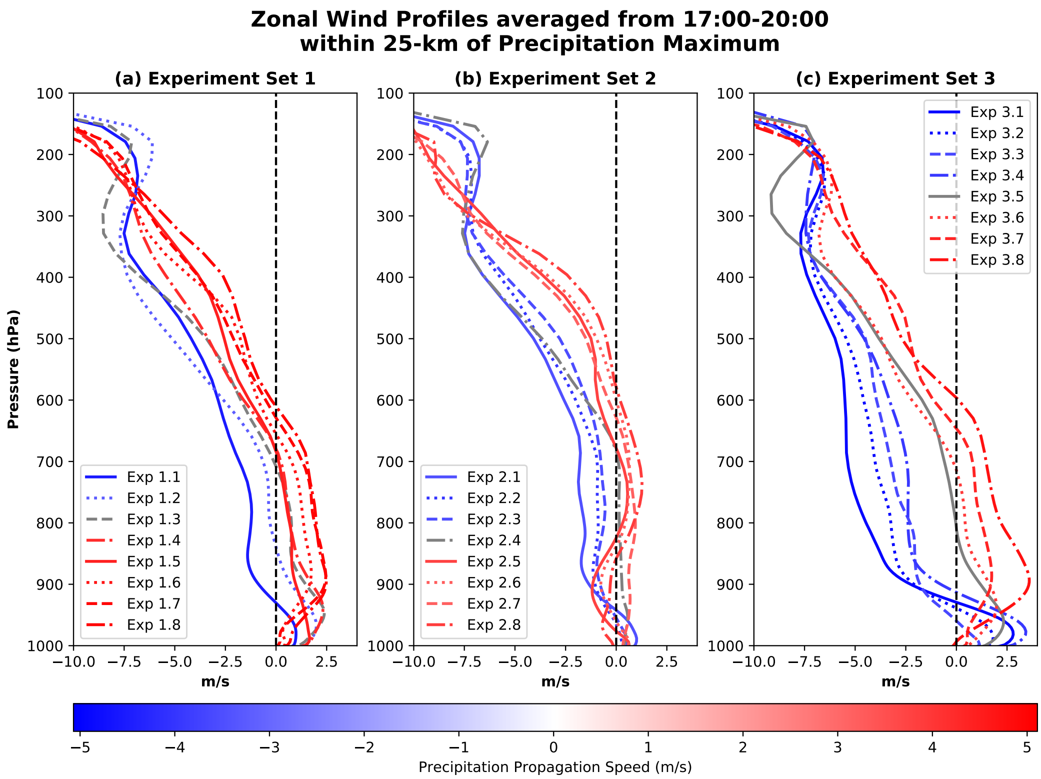

FIG. 14. (a) Zonal wind profiles averaged from 17:00-20:00 within 25-km of the average location of maximum precipitation between 17:00 and 20:00 in the composite, for sensitivity experiments set 1. (b) As in (a) but for sensitivity experiments set 2. (c) As in (a) but for sensitivity experiments set 3. Profiles are color coded by the propagation velocity of the smoothed (to 5-km spacing) maximum precipitation rate between 20:00 and 08:00 in each experiment, with red indicating eastward propagation, and blue indicating westward propagation. The gray profiles are chosen subjectively as experiments with weak or inconsistent offshore propagation in which the objective algorithm to calculate propagation speed failed.

reversal in the lower free troposphere, such that surface winds are in opposition to the low-level shear vector. In such and environment, storms could initiate on the leeward side of the island (relative to the low-level wind) and then propagate entirely across the island. This occurred in our experiments 2.5-2.8 and can be seen based on the location of precipitation initiation on the west side of the island in the early evening in Fig. 15, and the eastward propagation denoted in Fig. 13b.

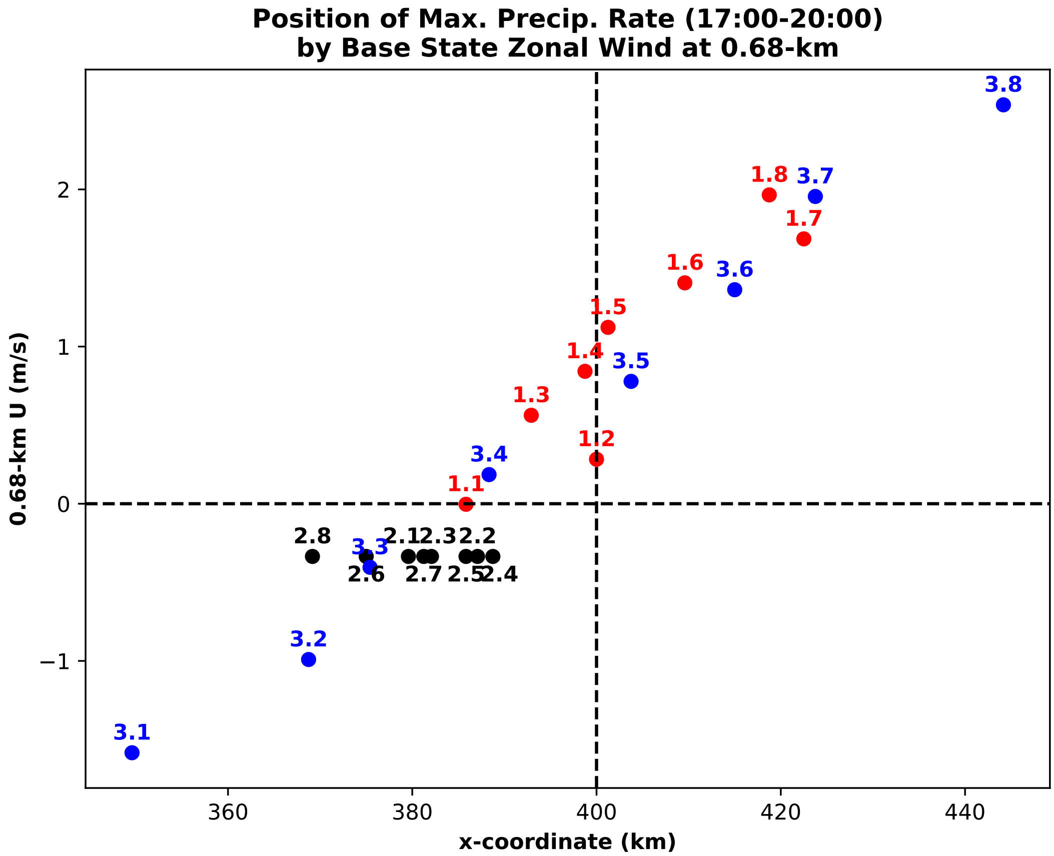

FIG. 15. The average longitudinal position of the maximum precipitation rate (after smoothing to 5-km spacing) between 17:00 and 20:00 is shown on the x-axis (in kilometers), with the base-state zonal wind (in m/s) at the 0.68-km above the surface on the y-axis. Dashed black lines indicate the center of the island (vertical) and 0 m/s (horizontal). The dots are color-coded by experiment set, with Set 1 in red, Set 2 in black, and Set 3 in blue. Each dot is also labelled with the corresponding experiment name.

5. Conclusions

This study has explored the impact of the environmental wind profile associated with different states of the monsoon-background on the diurnal cycle of precipitation. We have used Luzon Island in the northern Philippines as an observational test case to compare idealized modeling results of a 200-km wide island. It is shown that consideration of the environmental wind alone can explain many features in the observed variability of the diurnal cycle. These results complement the findings of many prior studies exploring the link between the diurnal cycle and large-scale modes of variability such as the MJO (e.g. Vincent and Lane 2016; Natoli and Maloney 2019; Short et al. 2019; Riley Dellaripa et al. 2020; Sakaeda et al. 2020), and also add to the general understanding of the diurnal cycle and offshore propagation of convection (Hassim et al. 2016; Kilpatrick et al. 2017; Yokoi et al. 2017, 2019). The main findings of this study are summarized as follows:

- Observed composite diurnal cycles conditioned on the environmental wind alone can capture distinct variability in diurnal cycle behavior. Strong diurnal cycles tend to occur with weak, offshore prevailing wind (Fig. 5b-f). Strong wind in either direction appears to be associated with a suppressed diurnal cycle (Fig. 5a,g).

- While westward propagation of diurnally generated convection is apparent in an observed composite of all days in the JJAS monsoon season (e.g. Natoli and Maloney 2019; Lee et al. 2021), this occurs primarily on days with the background wind more easterly than average (-1.5, -1.0, -0.5σ bins in Fig. 6a-c).

- A simple, 2-D idealized simulation using CM1 can replicate the direction of propagation and qualitative strength of diurnally generated convection as impacted by the background wind that is seen in observations (Figs. 6 and 8)

- Strong background winds can ventilate the land surface and reduce the land-sea contrast, particularly on the windward side of the island, and greatly reduce the sea-breeze strength (Figs. 9 and 11). A sea-breeze can still be identified on the leeward side of the island, but even this is reduced under the strongest winds.

- Convection propagates offshore during the overnight hours in the direction of the wind between 700-900-hPa, but moves at a speed of 3-6 m/s, consistent with density current speeds (Figs. 8 and 13).

These results improve understanding of the large-scale controls on the diurnal cycle in and near tropical islands, and are applicable to the study of the MJO/BSISO-diurnal cycle relationship. We have shown that the background wind alone can explain several aspects of diurnal cycle variability attributed to the MJO. For example, the direction of offshore propagation appears to be determined by the wind in the lower free-troposphere (Figs. 8 and 13), consistent with Ichikawa and Yasunari

(2006, 2008), Fujita et al. (2011), and Ruppert and Zhang (2019). Light, offshore winds appear to be associated with the strongest diurnal cycles both in observations (Fig. 5) and our idealized CM1 simulations (Figs. 8 and 2), favoring strong diurnally generated convection on the leeward side of an island (Fig. 15). This supports findings by Virts et al. (2013), Natoli and Maloney (2019), Sakaeda et al. (2020), and Qian (2020), among others, who have identified heavy diurnal precipitation during the transition from suppressed to active MJO state, particularly on the west side of large islands (which is in the lee before the westerly wind burst arrives later in the active phase). The reduction in land-sea contrast shown in Fig. 11 supports the hypothesis that the onshore wind during active phases of the MJO is an important reason why the diurnal cycle is suppressed (Short et al. 2019; Yokoi et al. 2019).

It is worth noting that many of these features from observations can be described in a 2-D model without topography. This is consistent with recent work that has suggested that topography is not vital in determining qualitative behavior of diurnally generated convection, although it can modestly increase the intensity of precipitation and modulate the timing of the diurnal cycle (Riley Dellaripa et al. 2020; Ruppert et al. 2020). Topography may also alter the precise location where convection forms on the island through interactions with the propagating sea breeze.

While the simplifications made in this study are attractive for getting to the base of the problem, there are some caveats that could affect interpretation of these results. These will be briefly outlined, along with some suggestions for avenues of future research. Offshore propagation of convection is symmetric between westward and eastward propagation (Fig. 8), while westward propagation is clearly dominant over eastward propagation in observations (Fig. 6). Since this cannot be replicated in these simulations, we are unable to test the mechanism producing this asymmetry. However, it is hypothesized that this is related to the asymmetry in the topography of Luzon, with the highest mountains concentrated near the west coast, and a much shorter mountain range on the east coast. The enhanced convergence contributed by the mountains concentrates precipitation near the west coast in the real atmosphere, and it is possible that the east coast range interferes with cold-pool and land-breeze dynamics, thus limiting eastward propagation. Additionally, Peatman et al. (2021) found that there can be some differences in diurnal cycle behavior associated with ambient wind between different islands, suggesting that the unique geography of an island may need to be considered when generalizing these results. In particular, the difference in diurnal cycle behavior on small islands has not been differentiated from that over the coasts of larger landmasses, such as the coast of Southeast Asia or Colombia. There is a possibility that some of the conclusions made in this dissertation are unique to CM1 and may not generalize to other more complex models such as WRF or RAMS. Our simulations are also unable to produce any oceanic precipitation not associated with offshore propagation, unlike the real atmosphere where the SCS experiences substantial rainfall around the clock during a monsoonal surge. Thus, our representation of the active phase may not be entirely realistic without temporal mean moisture convergence. Many of these caveats could be addressed with future research.

We have shown that prevailing wind speed and direction is vital to understanding the large-scale controls on tropical island diurnal cycle behavior, and the wind alone can explain many aspects of the widely studied MJO-diurnal cycle relationship. However, we have not yet addressed the effects of other aspects of the environment modulated by large-scale modes of variability. Model sensitivity tests are ongoing to explore the contributions of several environmental background conditions, such as the ambient moisture and morning insolation, to diurnal cycle variability on tropical islands such as Luzon. We expect this will provide additional insight on the importance of the background wind relative to other variables in determining the behavior of the diurnal cycle on tropical islands and its offshore propagation.

Acknowledgments. This work forms part of the Ph.D. dissertation of Michael Natoli. This work was supported by the Office of Naval Research (ONR) under the Propagation of Tropical Intraseasonal Oscillations (PISTON) project N00014-16-1-3087, the NOAA CVP program under grant NA18OAR4310299, NASA CYGNSS grant 80NSSC21K1004, and the Climate and Large Scale Dynamics Program of the National Science Foundation under grant AGS-1735978. The authors would like to thank Prof. Susan van den Heever, Dr. Leah Grant, and Prof. Russ Schumacher at Colorado State University for their helpful advice and guidance in designing and running the model experiments.

Data availability statement. CMORPH bias-corrected precipitation data as described in Xie et al. (2017) can be downloaded at https://www.ncei.noaa.gov/data/cmorph-high-resolution-global-precipitation-estimates/access/30min/8km/. ERA5 data as described in Hersbach et al. (2020) can be download at https://www.ecmwf.int/en/forecasts/datasets/reanalysis-datasets/era5. The code for

CM1 can be downloaded from https://www2.mmm.ucar.edu/people/bryan/cm1/. Output from the simulations described in this study will be made available upon request to the authors.

References

Annamalai, H., and J. M. Slingo, 2001: Active / break cycles: diagnosis of the intraseasonal variability of the Asian Summer Monsoon. *Climate Dyn.*, **18**, 85–102.

Aves, S. L., and R. H. Johnson, 2008: The diurnal cycle of convection over the northern South China Sea. *J. Meteor. Soc. Japan*, **86**, 919–934.

Bai, H., and Coauthors, 2021: Formation of offshore rainfall near the west coast of Sumatra: Land breeze or gravity wave? *Mon. Wea. Rev.*, **149**, 715–731.

Bergemann, M., C. Jakob, and T. P. Lane, 2015: Global detection and analysis of coastline-associated rainfall using an objective pattern recognition technique. *J. Climate*, **28**, 7225–7236.

Biasutti, M., S. E. Yuter, C. D. Burleyson, and A. H. Sobel, 2012: Very high resolution rainfall patterns measured by TRMM Precipitation Radar: Seasonal and diurnal cycles. *Climate Dyn.*, **39**, 239–258.

Bryan, G. H., and J. M. Fritsch, 2002: A benchmark simulation for moist nonhydrostatic numerical models. *Mon. Wea. Rev.*, **130**, 2917–2928.

Bryan, G. H., and H. Morrison, 2012: Sensitivity of a simulated squall line to horizontal resolution and parameterization of microphysics. *Mon. Wea. Rev.*, **140**, 202–225.

Carbone, R. E., J. W. Wilson, T. D. Keenan, and J. M. Hacker, 2000: Tropical island convection in the absence of significant topography. Part I: Life cycle of diurnally forced convection. *Mon. Wea. Rev.*, **128**, 3459–3480.

Chen, T.-C., and K. Takahashi, 1995: Diurnal variation of outgoing longwave radiation in the vicinity of the South China Sea: Effect of intraseasonal oscillation. *Mon. Wea. Rev.*, **123**, 566–577.

Chen, X., F. Zhang, and J. H. Ruppert, 2019: Modulations of the diurnal cycle of coastal rainfall over south China caused by the Boreal Summer Intraseasonal Oscillation. *J. Climate*, **32**, 2089–2108.

Chen, X., F. Zhang, and K. Zhao, 2017: Influence of monsoonal wind speed and moisture content on intensity and diurnal variations of the Mei-Yu season coastal rainfall over south China. *J. Atmos. Sci.*, **74**, 2835–2856.

Chudler, K., W. Xu, and S. A. Rutledge, 2020: Impact of the Boreal Summer Intraseasonal Oscillation on the diurnal cycle of precipitation near and over the island of Luzon. *Mon. Wea. Rev.*, **148**, 1805–1827.

Copernicus Climate Change Service (C3S), 2017: ERA5: Fifth generation of ECMWF atmospheric reanalyses of the global climate. Copernicus Climate Change Service Climate Data Store (CDS), URL https://cds.climate.copernicus.eu/cdsapp#!/home, accessed 16 February 2021.

Dai, A., 2001: Global precipitation and thunderstorm frequencies. Part II: Diurnal variations. *J. Climate*, **14**, 1112–1128.

Durran, D. R., and J. B. Klemp, 1983: A compressible model for the simulation of moist mountain waves. *Mon. Wea. Rev.*, **111**, 2341–2361.

Ferrett, S., G.-Y. Yang, S. J. Woolnough, J. Methven, K. Hodges, and C. E. Holloway, 2019: Linking extreme preciptiation in Southeast Asia to equatorial waves. *Quart. J. Roy. Meteor. Soc.*, **146**, 665–684.

Finkele, K., 1998: Inland and offshore propagation speeds of a sea breeze from simulations and measurements. *Bound.-Layer Meteor.*, **87**, 307–329.

Fujita, M. K., K. Yoneyama, S. Mori, T. Nasuno, and M. Satoh, 2011: Diurnal convection peaks over the eastern Indian Ocean off Sumatra during different MJO phases. *J. Meteor. Soc. Japan*, **89A**, 317–330.

Gill, A. E., 1980: Some simple solutions for heat-induced tropical circulation. *Quart. J. Roy. Meteor. Soc.*, **106**, 447–462.

Gilman, D. L., F. J. Fuglister, and J. M. M. Jr., 1963: On the power spectrum of "Red Noise". *J. Atmos. Sci.*, **20**, 182–184.

Grant, L. D., T. P. Lane, and S. C. van den Heever, 2018: The role of cold pools in tropical oceanic convective systems. *J. Atmos. Sci.*, **75**, 2615–2634.

Grant, L. D., M. W. Moncrieff, T. P. Lane, and S. C. van den Heever, 2020: Shear-parallel tropical convective systems: Importance of cold pools and wind shear. *Geophys. Res. Lett.*, **47**, e2020GL087 720.

Grant, L. D., and S. C. van den Heever, 2016: Cold pool dissipation. *J. Geophys. Res. Atmos.*, **121**, 1138–1155.

Hagos, S. M., C. Zhang, Z. Feng, C. D. Burleyson, C. DeMott, B. Kerns, J. J. Benedict, and M. N. Martini, 2016: The impact of the diurnal cycle on the propagation of Madden-Julian Oscillation convection across the Maritime Continent. *J. Adv. Model. Earth Syst.*, **8**, 1552–1564.

Hassim, M. E. E., T. P. Lane, and W. W. Grabowski, 2016: The diurnal cycle of rainfall over New Guinea in convection-peritting WRF simulations. *Atmos. Chem. Phys.*, **16**, 161–175.

Hersbach, H., and Coauthors, 2020: The ERA5 global reanalysis. *Quart. J. Roy. Meteor. Soc.*, **146**, 1999–2049.

Ho, C.-H., M.-S. Park, Y.-S. Choi, and Y. N. Takayabu, 2008: Relationship between intraseasonal oscillation and diurnal variation of summer rainfall over the South China Sea. *Geophys. Res. Lett.*, **35**, L03 701.

Hong, S.-Y., Y. Noh, and J. Dudhia, 2006: A new vertical diffusion package with an explicit tratment of entrainment processes. *Mon. Wea. Rev.*, **134**, 2318–2341.

Houze, R. A., S. G. Geotis, F. D. M. Jr., and A. K. West, 1981: Winter monsoon convection in the vicinity of north Borneo. Part I: Structure and time variation of the clouds and precipitation. *Mon. Wea. Rev.*, **109**, 1595–1614.

Ichikawa, H., and T. Yasunari, 2006: Time-space characteristics of diurnal rainfall over Borneo and surrounding oceans as observed by TRMM-PR. *J. Climate*, **19**, 1238–1260.

Ichikawa, H., and T. Yasunari, 2008: Intraseaonal variability in diurnal rainfall over New Guinea and the surrounding oceans during austral summer. *J. Climate*, **21**, 2852–2868.

Jiménez, P. A., J. Dudhia, J. F. González-Ruoco, J. Navarro, J. P. Montávez, and E. García-Bustamante, 2012: A revised scheme for the WRF surface layer formulation. *Mon. Wea. Rev.*, **140**, 898–918.

Joyce, R. J., J. E. Janowiak, P. A. Arkin, and P. Xie, 2004: CMORPH: A method that produces global precipitation estimates from passive microwave and infrared data at high spatial and temporal resolution. *J. Hydrometeor.*, **5**, 487–503.

Keenan, T. D., and R. E. Carbone, 1992: A preliminary morphology of precipitation systems in tropical northern Australia. *Quart. J. Roy. Meteor. Soc.*, **118**, 283–326.

Kikuchi, K., and B. Wang, 2008: Diurnal precipitation regimes in the global tropics. *J. Climate*, **21**, 2680–2696.

Kilpatrick, T., S.-P. Xie, and T. Nasuno, 2017: Diurnal convection-wind coupling in the Bay of Bengal. *J. Geophys. Res.*, **122**, 9705–9720.

Knapp, K. R., H. J. Diamond, J. P. Kossin, M. C. Kruk, and C. J. Schreck, 2018: NCDC International Best Track Archive for Climate Stewardship (IBTrACS) Project, Version 4. NOAA National Centers for Environmental Information, accessed 8 July 2021.

Knapp, K. R., M. C. Kruk, D. H. Levinson, H. J. Diamond, and C. J. Neumann, 2010: The International Best Track Archive for Climate Stewardship (IBTrACS): Unifying tropical cyclone best track data. *Bull. Amer. Meteor. Soc.*, **91**, 363–376.

Lafore, J.-P., and M. W. Moncrieff, 1989: A numerical investigation of the organization and interaction of the convective and stratiform regions of tropical squall lines. *J. Atmos. Sci.*, **46**, 521–544.

Lane, T. P., and F. Zhang, 2011: Coupling between gravity waves and tropical convection at mesoscales. *J. Atmos. Sci.*, **68**, 2582–2598.

Lee, C.-A., W.-R. Huang, Y.-H. Chang, and S.-M. Huang, 2021: Impact of multiple-scale circulation interactions on the spring diurnal precipitation over Luzon. *Sci. Rep.*, **11**, 9937.

LeMone, M. A., G. M. Barnes, and E. J. Zipser, 1984: Momentum flux by lines of cumulonimbus over the tropical oceans. *J. Atmos. Sci.*, **41**, 1914–1932.

Liang, Z., and D. Wang, 2017: Sea breeze and precipitation over Hainan Island. *Quart. J. Roy. Meteor. Soc.*, **143**, 137–151.

Liang, Z., D. Wang, Y. Liu, and Q. Cai, 2017: A numerical study of the convection triggering and propagation associated with sea breeze circulation over Hainan Island. *J. Geophys. Res. Atmos.*, **122**, 8567–8592.

Liu, C., and M. W. Moncrieff, 1996: A numerical study of the effects of ambient flow and shear on density currents. *Mon. Wea. Rev.*, **124**, 2282–2303.

Love, B. S., A. J. Matthews, and G. M. S. Lister, 2011: The diurnal cycle of precipitation over the Maritime Continent in a high resolution f model. *Quart. J. Roy. Meteor. Soc.*, **137**, 934–947.

Lu, J., T. Li, and L. Wang, 2019: Precipitation diurnal cycle over the Maritime Continent modulated by the MJO. *Clim. Dyn.*, **53**, 6489–6501.

Madden, R. A., and P. R. Julian, 1971: Detection of a 40-50 day oscillation in the zonal wind in the tropical Pacific. *J. Atmos. Sci.*, **28**, 702–708.

Madden, R. A., and P. R. Julian, 1972: Description of global-scale circulation cells in the tropics with a 40-50 day period. *J. Atmos. Sci*, **29**, 1109–1123.

Madden, R. A., and P. R. Julian, 1994: Observations of the 40–50-Day tropical oscillation - A review. *Mon. Wea. Rev.*, **22**, 813–837.

Maloney, E. D., and D. L. Hartmann, 1998: Frictional moisture convergence in a composite life cycle of the Madden-Julian oscillation. *J. Climate*, **11**, 2387–2403.

Mapes, B. E., T. T. Warner, and M. Xu, 2003: Diurnal patterns of rainfall in northwestern South America. Part III: Diurnal gravity waves and nocturnal convection offshore. *Mon. Wea. Rev.*, **131**, 830–844.

Matsumoto, J., L. M. P. Olaguera, D. Nguyen-Le, H. Kubota, and M. Q. V. II, 2020: Climatological seasonal changes of wind and rainfall in the Philippines. *Int. J. Climatol.*, **40**, 4843–4857.

Mori, S., J.-I. Hamada, Y. I. Tauhid, and M. D. Yamanaka, 2004: Diurnal land-sea rainfall peak migration over Sumatera island, Indonesian Maritime Continent, observed by TRMM satellite and intensive rawinsonde soundings. *Mon. Wea. Rev.*, **132**, 2021–2039.

National Geophysical Data Center, 2006: 2-minute Gridded Global Relief Data (ETOPO2)v2. NOAA, accessed 12 February 2018, https://doi.org/10.7289/V5J1012Q.

Natoli, M. B., 2022: Intraseasonal Variability in the Tropical Diurnal Cycle. Ph.D. thesis, Colorado State University, 164 pp., URL https://mountainscholar.org/handle/10217/235352.

Natoli, M. B., and E. D. Maloney, 2019: Intraseasonal variability of the diurnal cycle of precipitation in the Philippines. *J. Atmos. Sci.*, **76**, 3633–3654.

Natoli, M. B., and E. D. Maloney, 2021: Quasi-Biweekly Extensions of the Monsoon Winds and the Philippine Diurnal Cycle. *Mon. Wea. Rev.*, **149**, 3939–3960.

Neale, R., and J. Slingo, 2003: The Maritime Continent and its role in the global climate: A GCM study. *J. Climate*, **16**, 834–848.

Nicholls, M. E., R. H. Johnson, and W. R. Cotton, 1988: The sensitivity of two-dimensional simulations of tropical squall lines to environmental profiles. *J. Atmos. Sci.*, **45**, 3625–3649.

Oh, J.-H., B.-M. Kim, K.-Y. Kim, H.-J. Song, and G.-H. Lim, 2013: The impact of the diurnal cycle on the MJO over the Maritime Continent: a modeling study assimilating TRMM rain rate into global analysis. *Clim. Dyn.*, **40**, 893–911.

Oh, J.-H., K.-Y. Kim, and G.-H. Lim, 2012: Impact of MJO on the diurnal cycle of rainfall over the western Maritime Continent in the austral summer. *Climate Dyn.*, **38**, 1167–1180.

Park, M.-S., C.-H. Ho, J. Kim, and R. L. Elsberry, 2011: Diurnal circulations and their multi-scale interaction leading to rainfall over the South China Sea upstream of the philippines during intraseasonal monsoon westerly wind bursts. *Climate Dyn.*, **37**, 1483–1499.

Peatman, S. C., A. J. Matthews, and D. P. Stevens, 2014: Propagation of the Madden-Julian Oscillation through the Maritime Continent and scale interaction with the diurnal cycle of precipitation. *Quart. J. Roy. Meteor. Soc.*, **140**, 814–825.

Peatman, S. C., J. Schwendike, C. E. Birch, J. H. Marsham, A. J. Matthews, and G.-Y. Yang, 2021: A Local-to-Large Scale View of Maritime Continent Rainfall: Control by ENSO, MJO, and Equatorial Waves. *J. Climate*, **34**, 8933–8953.

Peters, K., and C. Hohenegger, 2017: On the dependence of squall-line characteristics on surface conditions. *J. Atmos. Sci.*, **74**, 2211–2228.

Qian, J. H., 2020: Mechanisms for the dipolar patterns of rainfall variability over large islands in the Maritime Continent associated with the Madden-Julian oscillation. *J. Atmos. Sci.*, **77**, 2257–2278.

Ramage, C. S., 1968: Role of a tropical "Maritime Continent" in the atmospheric circulation. *Mon. Wea. Rev.*, **96**, 365–370.

Rauniyar, S. P., and K. J. E. Walsh, 2011: Scale interaction of the diurnal cycle of rainfall over the Maritime Continent and Australia: Influence of the MJO. *J. Climate*, **24**, 325–348.

Rauniyar, S. P., and K. J. E. Walsh, 2013: Influence of ENSO on the diurnal cycle of rainfall over the Maritime Continent and Australia. *J. Climate*, **26**, 1304–1321.

Riley, E. M., B. E. Mapes, and S. N. Tulich, 2011: Clouds associated with the Madden-Julian Oscillation: A new perspective from *CloudSat*. *J. Atmos. Sci.*, **68**, 3032–3051.

Riley Dellaripa, E. M., E. D. Maloney, B. A. Toms, S. M. Saleeby, and S. C. van den Heever, 2020: Topographic effects on the Luzon diurnal cycle during the BSISO. *J. Atmos. Sci.*, **77**, 3–30.

Rotunno, R., J. B. Klemp, and M. L. Weisman, 1988: A theory for strong, long-lived squall lines. *J. Atmos. Sci.*, **45**, 463–485.

Ruppert, J. H., and X. Chen, 2020: Island rainfall enhancement in the Maritime Continent. *Geophys. Res. Lett.*, **47**, e2019GL086 545.

Ruppert, J. H., X. Chen, and F. Zhang, 2020: Convectively forced diurnal gravity waves in the Maritime Continent. *J. Atmos. Sci.*, **77**, 1119–1136.

Ruppert, J. H., and F. Zhang, 2019: Diurnal forcing and phase locking of gravity waves in the Maritime Continent. *J. Atmos. Sci.*, **76**, 2815–2835.

Saito, K., T. Keenan, G. Holland, and K. Puri, 2001: Numerical simulation of the diurnal evolution of tropical island convection over the Maritime Continent. *Mon. Wea. Rev.*, **129**, 378–400.

Sakaeda, N., G. Kiladis, and J. Dias, 2020: The diurnal cycle of rainfall and the convectively coupled equatorial waves over the Maritime Continent. *J. Climate*, **33**, 3307–3331.

Sakurai, N., and Coauthors, 2005: Diurnal cycle of cloud system migration over sumatera island. *J. Meteor. Soc. Japan*, **83**, 835–850.

Shige, S., Y. Nakano, and M. K. Yamamoto, 2017: Role of orography, diurnal cycle, and intraseasonal oscillation in summer monsoon rainfall over the Western Ghats and Myanmar coast. *J. Climate*, **30**, 9365–9381.

Short, E., C. L. Vincent, and T. P. Lane, 2019: Diurnal cycle of surface winds in the Maritime Continent observed through satellite scatterometry. *Mon. Wea. Rev.*, **147**, 2023–2044.

Sui, C.-H., and K.-M. Lau, 1992: Multiscale phenomena in the tropical atmosphere over the western Pacific. *Mon. Wea. Rev.*, **120**, 407–430.

Tulich, S. N., and G. N. Kiladis, 2012: Squall lines and convectively coupled gravity waves in the tropics: Why do most cloud systems propagate westward? *J. Atmos. Sci.*, **69**, 2995–3012.

Vincent, C. L., and T. P. Lane, 2016: Evolution of the diurnal precipitation cycle with the passage of a Madden-Julian oscillation event through the Maritime Continent. *Mon. Wea. Rev.*, **144**, 1983–2005.

Vincent, C. L., and T. P. Lane, 2017: A 10-Year Austral summer climatology of observed and modeled intraseasonal, mesoscale, and diurnal variations over the Maritime Continent. *J. Climate*, **30**, 3807–3828.

Vincent, C. L., and T. P. Lane, 2018: Mesoscale variation in diabatic heating around Sumatra, and its modulation with the Madden-Julian Oscillation. *Mon. Wea. Rev.*, **146**, 2599–2614.

Virts, K. S., J. M. Wallace, M. L. Hutchins, and R. H. Holzworth, 2013: Diurnal lightning variability over the Maritime Continent: Impact of low-level winds, cloudiness, and the MJO. *J. Atmos. Sci.*, **70**, 3128–3146.

Wang, B., and X. Xu, 1997: Northern Hemisphere summer monsoon singularities and climatological intraseasonal oscillation. *J. Climate*, **10**, 1071–1085.

Wang, S., and A. H. Sobel, 2017: Factors controlling rain on small tropical islands: Diurnal cycle, large-scale wind speed, and topography. *J. Atmos. Sci.*, **74**, 3515–3532.

Wu, P., D. Ardiansyah, S. Yokoi, S. Mori, F. Syamsudin, and K. Yoneyama, 2017: Why torrential rain occurs on the western coast of Sumatra island at the leading edge of the MJO westerly wind bursts. *SOLA*, **13**, 36–40.

Xie, P., R. Joyce, S. Wu, S.-H. Yoo, Y. Yarosh, F. Sun, and R. Lin, 2017: Reprocessed, bias-corrected CMORPH global high-resolution precipitation estimates from 1998. *J. Hydrometeor.*, **18**, 1617–1641.

Xu, W., and S. A. Rutledge, 2018: Convective variability associated wit the Boreal Summer Intraseasonal Oscillation in the South China Sea region. *J. Climate*, **31**, 7363–7383.

Xu, W., S. A. Rutledge, and K. Chudler, 2021: Diurnal cycle of coastal convection in the South China Sea Region and modulation by the BSISO. *J. Climate*, **34**, 4297–4314.

Yanase, A., K. Yasunaga, and H. Masunaga, 2017: Relationship between the direction of diurnal rainfall migration and the ambient wind over the southern Sumatra island. *Earth and Space Science*, **4**, 117–127.

Yang, G.-Y., and J. Slingo, 2001: The diurnal cycle in the tropics. *Mon. Wea. Rev.*, **129**, 784–801.

Yokoi, S., S. Mori, M. Katsumata, B. Geng, K. Yasunaga, F. Syamsudin, Nurhayati, and K. Yoneyama, 2017: Diurnal cycle of precipitatio observed in the western coastal area of Sumatra island: Offshore preconditioning by gravity waves. *Mon. Wea. Rev.*, **145**, 3745–3761.

Yokoi, S., S. Mori, F. Syamsudin, U. Haryoko, and B. Geng, 2019: Environmental conditions for nighttime offshore migration of precipitation area as revealed by in situ observation off Sumatra Island. *Mon. Wea. Rev.*, **147**, 3391–3407.

Zhong, S., and E. S. Takle, 1993: The effects of large-scale winds on the sea-land-breeze circulations in an area of complex coastal heating. *J. Appl. Meteor.*, **32**, 1181–1195.

Zhu, L., Z. Meng, F. Zhang, and P. M. Markowski, 2017: The influence of sea- and land-breeze circulations on the diurnal variability in precipitation over a tropical island. *Atmos. Chem. Phys.*, **17**, 13 213–13 232.